

# Optical caustics of Kerr spacetime: the full structure

V. Bozza<sup>a,b</sup>

<sup>a</sup> *Dipartimento di Fisica “E.R. Caianiello”, Università di Salerno, via Allende, I-84081 Baronissi (SA), Italy.*

<sup>b</sup> *Istituto Nazionale di Fisica Nucleare, Sezione di Napoli.*

(Dated: September 30, 2018)

We present an exhaustive numerical investigation of the optical caustics in gravitational lensing by a spinning black hole for an observer at infinity. Besides the primary caustic, we examine higher order caustics, formed by photons performing one or several loops around the black hole. Our investigation covers the whole parameter space, including the black hole spin, its inclination with respect to the line of sight, the source distance, and the caustic order. By comparing our results with the available analytical approximations, we find perfect agreement in their respective domains of validity. We then prove that all caustics maintain their shape (a tube with astroidal cross-section) in the entire parameter space without suffering any transitions to different caustic shapes. For nearly extremal spin, however, higher order caustics grow so large that their cross-sections at fixed radii wind several times around the black hole. As a consequence, for each caustic order, the number of images ranges from 2 to  $2(n + 1)$ , where  $n$  is the number of loops spanned by the caustic. As for the critical curves, we note that for high values of the spin they develop a small dip on the side corresponding to prograde orbits.

PACS numbers: 95.30.Sf, 04.70.Bw, 98.62.Sb

Keywords: Relativity and gravitation; Classical black holes; Gravitational lensing

## I. INTRODUCTION

If General Relativity is the correct theory of gravity, the Kerr solution describes the spacetime metric outside spinning black holes [1]. Therefore it is currently utilized in all models trying to reconstruct the phenomena observed around observed astrophysical black holes, either remnants of stellar collapse or supermassive black holes lying in the central regions of several galaxies [2, 3]. A crucial step in the comprehension of physics in such extreme environments is the complete understanding of the phenomenology related to the bending of photon trajectories caused by spacetime curvature. In order to get reliable predictions on any observables, it is necessary to keep in mind that a Kerr black hole acts as a very strong gravitational lens, generating an infinite number of images of the same source [4]. The total flux of a source close to a Kerr black hole, (such as the accretion disk itself [5, 6], an isolated bright spot on it [7, 8] or a star orbiting the black hole [9]) gets a significant contribution from the secondary image and from higher order images [6]. This is also true for the details of fine structures in the profile of spectral lines, such as the iron  $K\alpha$  line in the X-ray domain, which are strong indicators of the presence of an intrinsic angular momentum of the black hole [10].

On the other hand, the progresses in radio [11] and infrared band [12] interferometry, along with the projects of X-ray interferometry in space (MAXIM, <http://maxim.gsfc.nasa.gov>), foreshadow that resolved pictures of the nearest supermassive black hole (Sgr A\* in the center of the Milky Way) will be feasible in a not so far future [13]. This will represent a spectacular advance in our knowledge of black hole physics. In particular, the contributions of different images of the same source

will be identified and studied separately. Higher order images will then provide a huge amount of independent information on the inner portions of the accretion disks of supermassive black holes and will become precious witnesses of the strong gravitational field just outside the horizon.

Gravitational lensing theory states that the multiplicity of the images of a given source depends on the source-lens-observer configuration. In a given spacetime metric, for an observer in a particular spacetime point, the multiplicity only depends on the source position. If the metric is stationary (as in the case of the Kerr metric) and the observer is static, the caustic can be defined in the 3-dimensional subspace at constant time as a 2-dimensional surface separating regions of space in which a source would give rise to a different number of images. When a point-like source crosses a caustic, a pair of additional images with infinite magnification is created or destroyed (the finite source size acts as a cut-off for real sources) [14].

It can be easily guessed that the study of the shape of the caustics is of fundamental importance for a reliable and complete description of the whole phenomenology related to the environment of astrophysical black holes. In fact, the multiplicity of the images and their brightness is essentially determined by the position of the source within the caustic structure. Even temporal variations in the observed overall luminosity may be due to caustic crossing of bright features around the black hole [15].

Surprisingly, 45 years after the discovery of the Kerr metric, the complete structure of the caustics of a spinning black hole has not yet been derived. Indeed, the complexity of the metric prevents from finding simple analytical solutions for the caustic surfaces. Even numerical studies are very challenging and not straightforward. The first indication of the existence of non-

degenerate caustics came from the work of Cunningham and Bardeen [9], who traced the light curves of a source star orbiting a spinning black hole. They noticed that the magnification of the primary and secondary images diverged at some particular points, signaling that caustic crossings were occurring. In spite of the huge number of ray-tracing codes in Kerr spacetime developed in so many years, the only comprehensive study of the caustic surfaces has been performed by Rauch and Blandford [15]. They have explicitly shown that the primary caustic is a tube with a cross-section having the shape of an astroid (a closed curve with four cusps), which is very typical in gravitational lensing theory as soon as the spherical symmetry of the lens is broken by an external or internal perturbation. They have shown several pictures of the primary caustic and derived some simple asymptotic behaviors for its size. Besides the primary caustic, the authors have mentioned the existence of higher order caustics, but they have not shown any pictures of them, leaving several questions about the size and the shape of these caustics open. Later on, Sereno and De Luca have found an analytical approximation for the primary caustic valid for large source distances [16]. In a series of papers based on the strong deflection limit approximation [17], we have derived a perturbative analytical approximation describing the higher order caustics (but not the primary caustic) [18, 19, 20]. These approximations show that at low spin values the higher order caustics are still tubes with astroidal cross sections with increasing size. Basically, this is all we know about caustics in the Kerr spacetime.

All these studies provide several hints about the caustic structure of the Kerr black hole lens in several limits. Yet, the fate of the higher order caustics at high values of the spin still remains unclear. As they become larger and larger with increasing spin, do they undergo any transitions to different caustic shapes? Does their size stay finite? Do they merge? The present work provides clear answers to these and other questions of theoretical and observational relevance, clarifying the whole panorama of the caustic structure of the Kerr spacetime. We present a thorough numerical analysis of the caustics generated by a Kerr black hole at all caustic orders, studying their dependence on the black hole spin, its inclination and the source distance. The reliability of our results is also double-checked against former studies and all analytical approximations available up to now.

The paper is organized as follows. Section II traces the methodology followed for the generation of the caustics, referring to the appendix for a detailed explanation of all steps. Section III deals with the primary caustic. Section IV discusses the dependence of higher order caustics on the spin and its inclination. Section V focuses on the caustics of extremal black holes. Section VI is devoted to critical curves in the observer's sky. Section VII contains the conclusions.

## II. METHODOLOGY

The Kerr metric in Boyer-Lindquist coordinates [21] is ( $G = c = 1$ )

$$ds^2 = \left(1 - \frac{2Mr}{\rho^2}\right) dt^2 - \frac{\rho^2}{\Delta} dr^2 - \rho^2 d\vartheta^2 - \left[\Delta + \frac{2Mr(r^2 + a^2)}{\rho^2}\right] \sin^2 \vartheta d\phi^2 + \frac{4aMr \sin^2 \vartheta}{\rho^2} dt d\phi \quad (1)$$

$$\Delta = r^2 - 2Mr + a^2, \quad (2)$$

$$\rho^2 = r^2 + a^2 \cos^2 \vartheta. \quad (3)$$

$M$  is the mass of the black hole and  $a$  is the specific angular momentum, ranging from 0 (Schwarzschild black hole) to  $M$  (extremal black hole). The horizon radius is  $r_h = M + \sqrt{M^2 - a^2}$ .

Let us consider a static observer at coordinates  $(r_o, \vartheta_o, \phi_o)$  with  $\phi_o = 0$  and let us assume  $r_o \gg 2M$  for simplicity. In practice, all astrophysical situations satisfy this limit. The observer's polar coordinate  $\vartheta_o$  also coincides with the inclination of the spin axis with respect to the line of sight between the observer and the black hole. It is often convenient to work with the coordinate  $\mu \equiv \cos \vartheta$  instead of  $\vartheta$ . Therefore, one can define  $\mu_o \equiv \cos \vartheta_o$ .

Similarly, we consider a source at coordinates  $(r_s, \vartheta_s, \phi_s)$ , with  $\mu_s \equiv \cos \vartheta_s$ .

The observer can construct his own coordinates  $(\theta_1, \theta_2)$  in the sky, such that the black hole is in the origin and the  $\theta_2$  axis coincides with the projection of the spin of the black hole on the sky.

Now we make a qualitative summary of the numerical algorithm for finding the caustics and state a few basic equations that should be sufficient to understand the main points. In Appendix A we report all the details of the calculation and the definitions of all variables.

The first important concept to be reviewed is the shadow of the black hole [2]. Imagine tracing a photon trajectory from the observer back toward the black hole. The trajectory is completely determined by the angles  $\theta_1$  and  $\theta_2$ , which specify the final direction of the photon when it hits the observer. These angles may be considered as the initial conditions for tracing back the photon geodesic in the Kerr metric. Then, it is well-known that there exists a set of photon trajectories that are traced back to grazing unstable fixed radii orbits around the black hole. These particular trajectories define a locus in  $(\theta_1, \theta_2)$ , which is called the shadow border of the black hole. As evident from Fig. 1, in the limit  $a \rightarrow 0$ , this locus has a circular shape with angular radius  $3\sqrt{3}M/r_o$ . For non-vanishing spin, it is slightly displaced toward the right direction (remember that we have chosen coordinates such that the spin of the black hole is projected on the positive  $\theta_2$  axis) and becomes slightly flattened on the left side. The shape of the shadow depends on

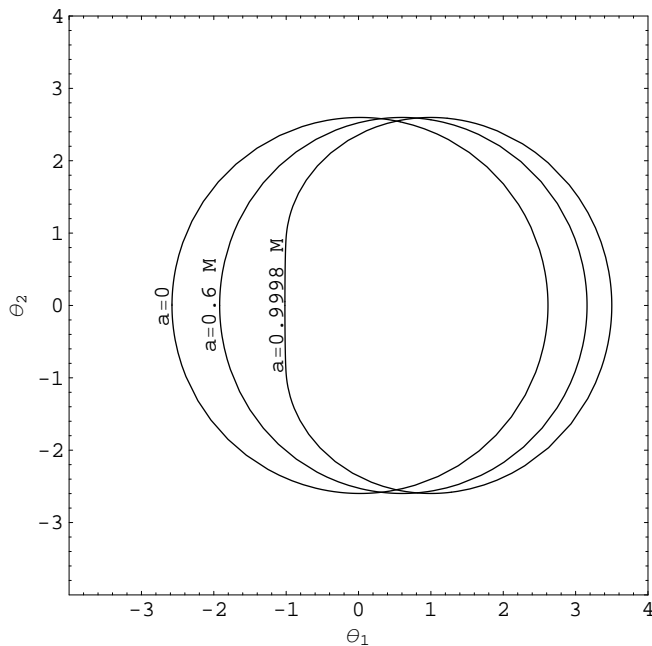


FIG. 1: The shadow border as seen by an equatorial observer for different values of the black hole spin.  $\theta_1$  and  $\theta_2$  are the angular coordinates in the observer’s sky in units of  $2M/r_o$ . The black hole is in the origin and the spin axis points in the positive  $\theta_2$  direction.

the black hole spin and its inclination on the line of sight and can be used, in principle, to extract these parameters [2, 13, 22]. The reason for the name “shadow border” is that all sources lying outside the unstable circular orbits generate images appearing outside this locus in the observer’s sky. Only sources very close to the black hole may have images inside the shadow border. Therefore, to an instrument with the sufficient angular resolution, the black hole should appear as a dark spot (shadow) surrounded by a more luminous region [13]. In the appendix, we review the derivation of the shape of the shadow border, which is explicitly given by Eqs. (A11) and (A12) in parametric form as functions of  $r_m$ , which represents the radius of the unstable photon orbit from which the photon emerges and hits the observer at angles  $(\theta_1, \theta_2)$ .

It is convenient to switch from  $r_m$  to a more friendly parameter that we call  $\eta$  as defined by Eq. (A14).  $\eta$  is very similar to an angular variable: as it ranges in  $[-\pi, \pi]$ , the whole shadow border is spanned. The intersections with the  $\theta_1$  axis are at  $\eta = 0$  (with  $\theta_1 > 0$ ) and  $\eta = \pm\pi$  (with  $\theta_1 < 0$ ).  $\eta = \pi/2$  corresponds to a point close to the positive  $\theta_2$  axis and  $\eta = -\pi/2$  corresponds to a point close to the negative  $\theta_2$  axis. As the spin axis is projected to the positive  $\theta_2$  axis, we can deduce that photons reaching the observer from the left of the black hole ( $\eta \simeq \pm\pi$ ) come from orbits co-rotating with the black hole, whereas photons reaching the observer from the right of the black hole ( $\eta \simeq 0$ ) come from orbits rotating in the opposite sense with respect to the black hole. We shall often re-

fer to photons on co-rotating orbits as prograde photons and to photons on counter-rotating orbits as retrograde photons. Photons reaching the observer from above or below the black hole ( $\eta \simeq \pm\pi/2$ ) come from quasi-polar orbits.

The shadow border can be used to construct new coordinates  $(\psi, \eta)$  in the observer’s sky, such that the sky coordinates  $(\theta_1, \theta_2)$  can be re-expressed in terms of them

$$\theta_1 = \theta_1(\psi, \eta) \quad (4)$$

$$\theta_2 = \theta_2(\psi, \eta). \quad (5)$$

These coordinates are similar to polar coordinates, with  $\eta$  playing the role of the polar angle and  $\psi$  related to the modulus  $\sqrt{\theta_1^2 + \theta_2^2}$ . The choice of the precise form of the radial variable  $\psi$  as a function of  $\sqrt{\theta_1^2 + \theta_2^2}$  is done with the purpose of simplifying the numerical calculations, as will be explained in the following paragraphs.

A detailed study of the geodesics equations at fixed source distance  $r_s$  (see Appendix) provides the sought after relation between the source’s angular coordinates and the variables  $\psi$  and  $\eta$

$$\mu_s = \mu_s(\psi, \eta) \quad (6)$$

$$\phi_s = \phi_s(\psi, \eta). \quad (7)$$

As  $\psi$  and  $\eta$  determine the position of the images in the observer’s sky, Eqs. (6) and (7) represent the Kerr lens mapping.

Of course, the detailed expression of this mapping may become very involved and cumbersome to numerical calculations if one does not make a proper choice of the variable  $\psi$ . Luckily, the explicit form of the function  $\mu_s$  in Eq. (6) consists of an oscillating Jacobi elliptic function whose argument monotonically increases when  $\sqrt{\theta_1^2 + \theta_2^2}$  decreases. From the physical point of view, this means that the closer the photon passes to the black hole the larger is the number of oscillations in the polar motion it performs. Then, it is natural to define  $\psi$  as the argument of this Jacobi elliptic function. With this definition, the function  $\mu_s(\psi, \eta)$  resembles a sinusoid in  $\psi$ , with the amplitude of the oscillations determined by  $\eta$ .

With a suitable normalization of  $\psi$ , we can set the period of the Jacobi elliptic function to  $\Delta\psi = 2$ . In this way, we can establish the equivalence  $\mu_s = 0 \Leftrightarrow \psi = m$ , with  $m$  integer. Furthermore, the number of inversions in the polar motion of the photon from the source to the observer is  $m = [\psi + 1/2]$ , where by  $[x]$  we indicate the integer part of  $x$ . The precise definition of  $\psi$  is given by Eq. (A36), though it is necessary to go through a conspicuous portion of the appendix to understand all the details.

As long as the Jacobian determinant of the lens mapping is different from zero, the mapping is locally invertible and the number of images stays constant. Images can be created or destroyed only in the critical points where the Jacobian determinant vanishes. It turns out that for each value of  $m$  there is one Jacobian critical

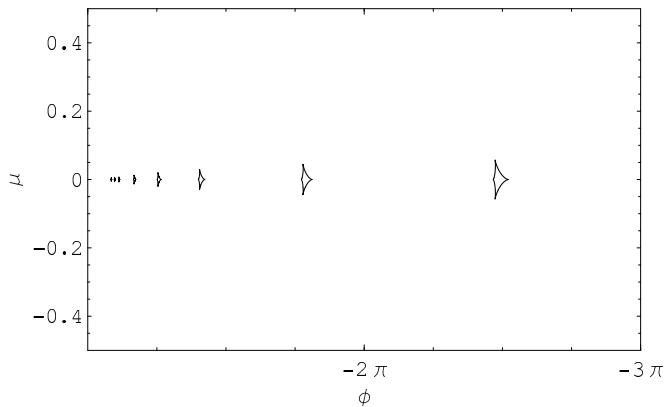


FIG. 2: Cross sections of the primary caustic for  $a = 0.9998M$  and  $\mu_o = 0$ . From left to right, the radial coordinate is  $r_s = 5M, 4.5M, 4M, 3M, 2.3M, 1.82M, 1.42M, 1.22M$ .

point in the interval between two consecutive polar inversions  $m - 1/2 < \psi < m + 1/2$ , for all values of  $\eta$ . Therefore, we can identify  $m$  with the caustic order. The primary caustic is obtained with a single polar inversion ( $m = 1$ ), the second order caustic is generated by photon trajectories with two polar inversions ( $m = 2$ ), and so on. With the critical points found in the  $(\psi, \eta)$  space, we can readily draw the critical curves in the observer's sky by applying Eqs. (4) and (5), and the caustics by applying Eqs. (6) and (7).

In conclusion, once we fix all the parameters (black hole spin  $a$ , spin inclination  $\mu_o$ , source distance  $r_s$ , caustic order  $m$ ), we are able to trace the corresponding caustic and critical curve through suitable numerical calculations.

### III. PRIMARY CAUSTIC

The primary caustic is the caustic generated by light rays with a single inversion point in the polar motion. In the Schwarzschild limit ( $a \rightarrow 0$ ), it degenerates to a line starting from the black hole and extending to infinity in the opposite direction with respect to the observer ( $\phi = -\pi$ ). Distant sources that approach the primary caustic experience the standard weak deflection gravitational lensing as described in classical textbooks. The two weak deflection images merge when the source lies right on the primary caustic, forming the well-known Einstein ring.

If we turn the black hole spin on, the degenerate one-dimensional caustic becomes a finite-thickness tube with a cross-section having the shape of a four-cusped astroid. Several cross-sections at fixed radii are shown in Fig. 2 for a nearly extremal Kerr black hole. If the source lies inside the enclosed region, two additional images are present

As already shown in the extensive study by Rauch & Blandford [15], the cross-section is reflection-symmetric

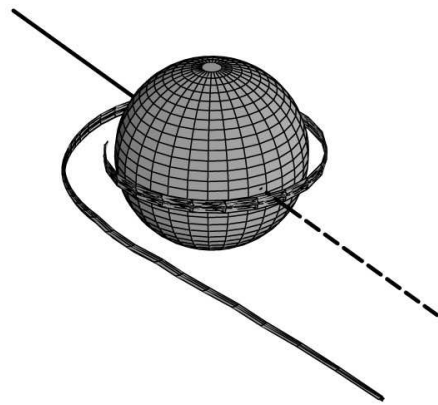


FIG. 3: The primary caustic tube for  $a = 0.9998M$  and  $\mu_o = 0$ . In building this 3-dimensional representation, we have chosen coordinates such that  $x = r \sin \vartheta \cos \phi$ ,  $y = r \sin \vartheta \sin \phi$ ,  $z = r \cos \vartheta$ , following Ref. [15]. The spin axis is directed toward the top. The straight solid line indicates the direction towards the observer, whereas the dashed line points in the opposite direction. The primary caustic for a Schwarzschild black hole ( $a = 0$ ) coincides with this dashed line.

at very large distances, but becomes more and more distorted approaching the black hole. Moreover, the caustic tube is shifted clockwise (i.e. in the sense opposite to the rotation of the black hole), as evident from Fig. 2, where it can be noted that the caustic does not lie at  $\phi = -\pi$ , as in the Schwarzschild case (We recall that we have put the observer in  $\phi_o = 0$ ). This shift becomes larger and larger for sources closer to the horizon. A full 3-dimensional picture of the primary caustic tube was first presented in Ref. [15] and is shown again here in Fig. 3. It can be noted that the caustic tube becomes belt-like as it winds around the black hole horizon, represented by the spherical surface in the figure.

As anticipated in the introduction, the caustic separates two regions of space in which a source gives rise to a different number of images. After drawing the primary caustic, it is useful to explain the way it affects the formation of the images around the corresponding critical curve. We remind the reader that only the images of order  $m = 1$  (i.e. generated by photons with one polar inversion) are involved.

In Fig. 4 we have drawn a schematic picture of the images of a source close to the caustic as detected by an observer. In Fig. 4a we have a cross-section of the primary caustic at  $r_s = 12M$ , along with several possible source positions, represented by different symbols. In Fig. 4b we show the corresponding critical curve as a solid line and the shadow border in dashed style. The images corresponding to the source positions of Fig. 4a are shown with the same symbol. We also remind the reader that the spin is directed toward the north pole ( $\mu = 1$ ) in Fig. 4a and is parallel to the  $\theta_2$  axis in Fig. 4b.

If the source is outside the caustic (the cross in Fig. 4a) there are two images (the two crosses in Fig. 4b). One

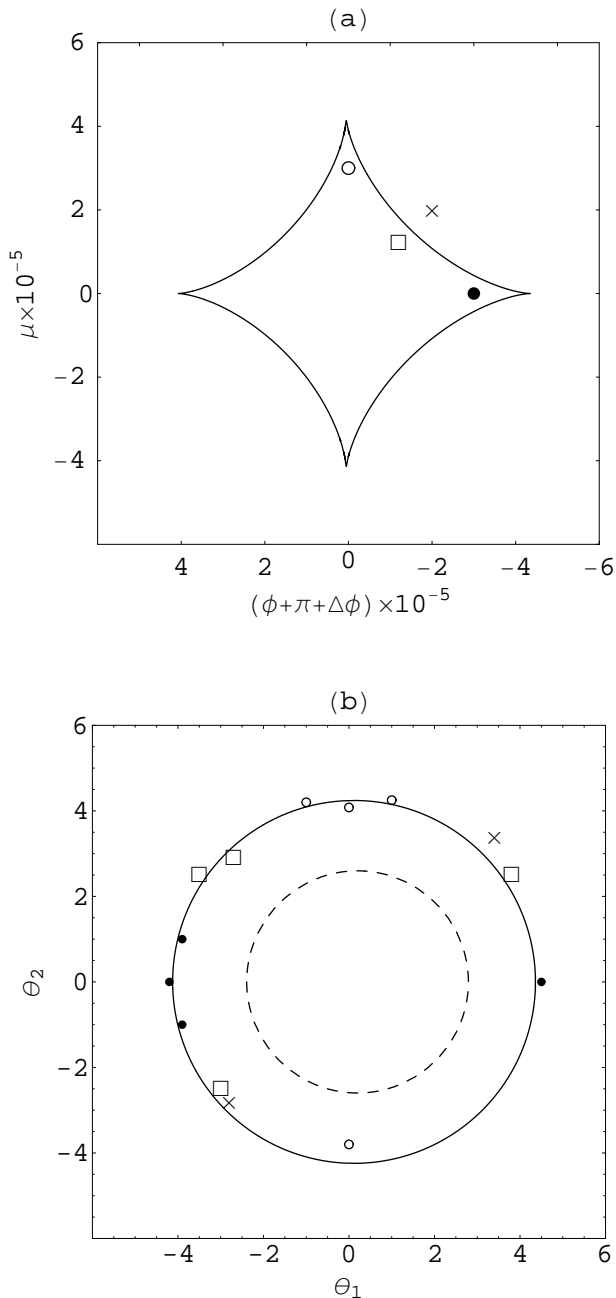


FIG. 4: A schematic picture of the images of a point-source at  $r_s = 12M$  generated by a black hole with spin  $a = 0.2M$  as seen by an equatorial observer. (a) The primary caustic cross-section and four possible positions of the source, indicated by the cross, the filled circle, the empty circle and the box. (b) The corresponding images in the observer's sky together with the critical curve (solid line) and the shadow of the black hole (dashed line).

image is on the same side of the source and lies outside the critical curve (primary image) and the other is opposite and lies inside the critical curve (secondary image). If the source enters the caustic from the right (empty box), two images with opposite parities are created on the left of the critical curve (there is a reflection with respect to a vertical axis from the caustic to the critical curve). If we place a source on the equatorial plane close to the right cusp (filled circle), we have three images close to the left tip of the critical curve, corresponding to prograde photons. Finally, if we have a source close to the upper cusp (empty circle), we have three images close to the upper tip of the critical curve.

Then, to summarize, the right cusp of the caustic involves the creation of images generated by prograde photons; the opposite occurs for the left cusp. Therefore, we will often refer to the right cusp as the prograde cusp and the left cusp as the retrograde cusp. As for the upper and lower cusps, they are associated with the formation of images generated by quasi-polar orbits. In the primary caustic (and in all odd higher order caustics), the upper cusp is associated with the upper tip of the critical curve, whereas in all even order caustics it is associated with the lower tip (there is also a reflection with respect to a horizontal axis in even order caustics [18]).

This picture is a useful reference to understand how the different parts of the caustic are associated with the the corresponding parts of the critical curve and where the images are created or destroyed when the source crosses a caustic. From now on, we will concentrate mostly on the shape of the caustics, confining the discussion about the critical curves to Section VI.

Coming back to the primary caustic surface, we find that for any values of the black hole spin the primary caustic performs an infinite number of turns around the horizon. This fact is evident from Fig. 5a, where the azimuthal coordinate of the left cusp (corresponding to retrograde photons) is plotted vs the logarithm of the difference between the radial coordinate and the horizon radius  $r_h$ . This plot shows that at large distances the primary caustic always tends to  $-\pi$ , whatever the value of the spin. In the opposite limit, very close to the black hole horizon, the position of the retrograde cusp shifts clockwise more and more without stopping ( $\phi$  increases with a negative sign). We can easily establish a logarithmic law  $\phi_c \simeq c(a) \log(r_s - r_h)$ , where the coefficient  $c(a)$  depends on the black hole spin, becoming larger and larger for high values of the spin.

As already guessed in Ref. [20], the divergence of the azimuthal position of the caustic in the approach to the horizon is a direct consequence of the divergence of the radial integral  $I_2$  (Eq. (A33) in the appendix) appearing in the lens equation for  $\phi_s$  (A38). This integral contains a factor  $1/\Delta$ , which generates the logarithmic divergence of  $I_2$ . This has been explicitly shown here by numerical calculations for the first time.

In Fig. 5b we plot the size of the primary caustic (calculated as the distance between the right and the left

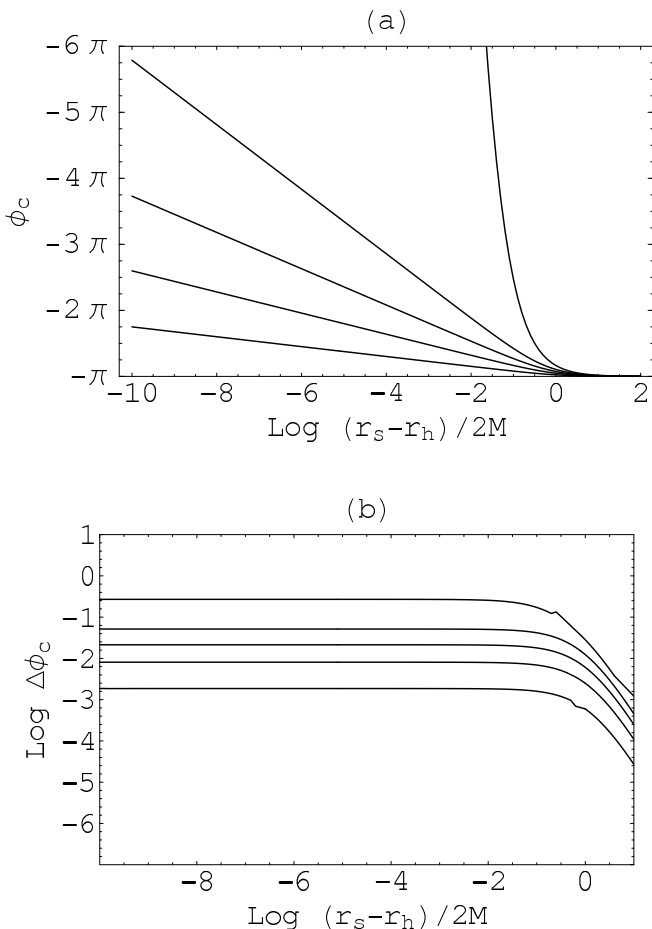


FIG. 5: (a) Azimuthal coordinate of the retrograde cusp of the primary caustic as a function of the radial coordinate. (b) Size of the primary caustic as a function of the radial coordinate. In both figures, from bottom to top, the curves are drawn for  $a = 0.2M, 0.4M, 0.6M, 0.8M, 0.9998M$ .

cusps) as a function of the radial coordinate in logarithmic scale. We see that the size tends to zero at very large distances, whatever the value of the spin. This is only true for the primary caustic, whereas all higher order caustics tend to a finite size at large distances, as we shall see in the next section. Close to the horizon, the size of the primary caustic tends to a constant.

Recently, an interesting analytical approximation for the primary caustic has been proposed by Sereno and De Luca in Ref. [16], using methods previously developed in Ref. [23]. This approximation is obtained by an expansion in the parameter

$$\varepsilon = \sqrt{\frac{M(r_o + r_s)}{4r_o r_s}}, \quad (8)$$

which is valid at large distances from the black hole for any values of the spin. The explicit expression of the

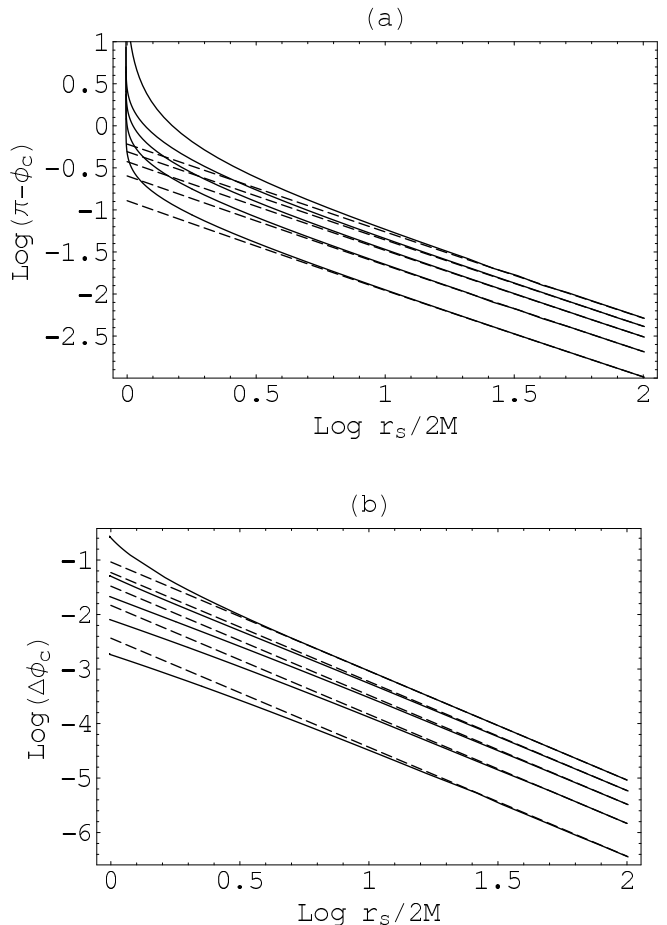


FIG. 6: Comparison between numerical calculations (solid lines) and the analytical approximation by Sereno and De Luca [16] (dashed lines). (a) Position of the retrograde cusp as a function of the radial coordinate. (b) Size of the caustic as a function of the radial coordinate. From bottom to top, the curves are for  $a = 0.2M, 0.4M, 0.6M, 0.8M, 0.9998M$ .

caustic reads

$$\begin{aligned} \phi_s &= -\pi - 4a\varepsilon^2 - \frac{5}{4}\pi a\varepsilon^3 \quad (9) \\ &+ \left[ \left( \frac{225}{128}\pi^2 - 16 \right) a - \frac{15}{16}\pi a^2 \sqrt{1 - \mu_o^2} \cos^3 \eta \right] \varepsilon^4 \\ \mu_s &= -\mu_o - \frac{15}{16}\pi a^2 (1 - \mu_o^2)^{3/2} \varepsilon^4 \sin^3 \eta, \quad (10) \end{aligned}$$

with  $\eta$  ranging from  $-\pi$  to  $\pi$ .

In Fig. 6 we compare our numerical results with the formulae by Sereno and De Luca, finding a perfect agreement at large distances from the black hole. In particular, Fig. 6a represents the azimuthal position of the retrograde cusp as a function of the radial coordinate in a log-log plot, whereas Fig. 6b shows the size of the caustic as a function of the radial coordinate in a log-log plot. The approximation only fails at very small distances from the horizon. It is interesting to note that the exact size is smaller than that predicted by Eq. (9) for small spins, whereas the situation is reversed at higher spins.

#### IV. HIGHER ORDER CAUSTICS

It is well-known that a Schwarzschild black hole generates two infinite sequences of lensed images of a given source [24]. Apart from the two main images, usually treated in the Weak Deflection Limit, all remaining images can be described in the Strong Deflection Limit [2, 17, 24]. Higher order images arise from the fact that photons grazing the unstable photon orbit may perform one or more turns around the black hole before emerging. For each turn, we have an additional pair of images, whose luminosity decreases exponentially as we increase the number of turns. In practice, gravitational lensing phenomenology is replicated for each number of turns around the black hole, including a new ring-like critical curve and a degenerate caustic line. Furthermore, the structure is replicated even for sources in front of the black hole (this geometrical configuration has been dubbed retro-lensing [25]). In this case, apart from the direct image of the source, all other images are due to strongly deflected photons turning around the black hole one or more times and reaching back the observer.

Standard lensing and retro-lensing caustics can be treated in a unified way, noting that we have a new caustic each time we add a new inversion point in the polar motion of the photon. As anticipated in Section II, the number of inversions can then be identified with the caustic order. For example, the primary caustic is generated by photons with a single inversion point, the second order caustic (first retro-lensing caustic) is generated by photons with two inversion points, the third order caustic (second standard lensing caustic) is generated by photons with three inversion points, and so on. This situation holds even when we switch the angular momentum on. Nevertheless, analogously to what happens for the primary caustic, higher order caustic tubes are shifted and acquire a finite thickness. Up to now, higher order caustics have been studied in the Strong Deflection Limit approximation [26] in the equatorial plane and successively for small values of the black hole spin in a fully analytical way [18, 19, 20]. In this section, we shall present a complete study of higher order caustics in the whole parameter space.

First we note that at large distances there is a fundamental difference between the primary caustic and the higher order caustics. In fact, whereas the primary caustic shrinks to zero size and tends to the Schwarzschild point-caustic at  $\phi = -\pi$  for  $r_s \rightarrow \infty$ , each higher order caustic tends to a well-determined asymptotic astroid shape in the coordinates  $(\phi, \mu)$ . Therefore, rather than a tube, at very large distances the 3-dimensional region enclosed by the caustic resembles a pyramid with astroidal base and vertex in the black hole. The volume enclosed within the caustic grows as  $\Omega_c r_s^2$ , where  $\Omega_c$  is the angular area within the asymptotic astroidal shape.

Let us begin by studying the dependence of the asymptotic cross-sections of the caustics at very large distances on the black hole spin  $a$ . In Fig. 7 we show the second

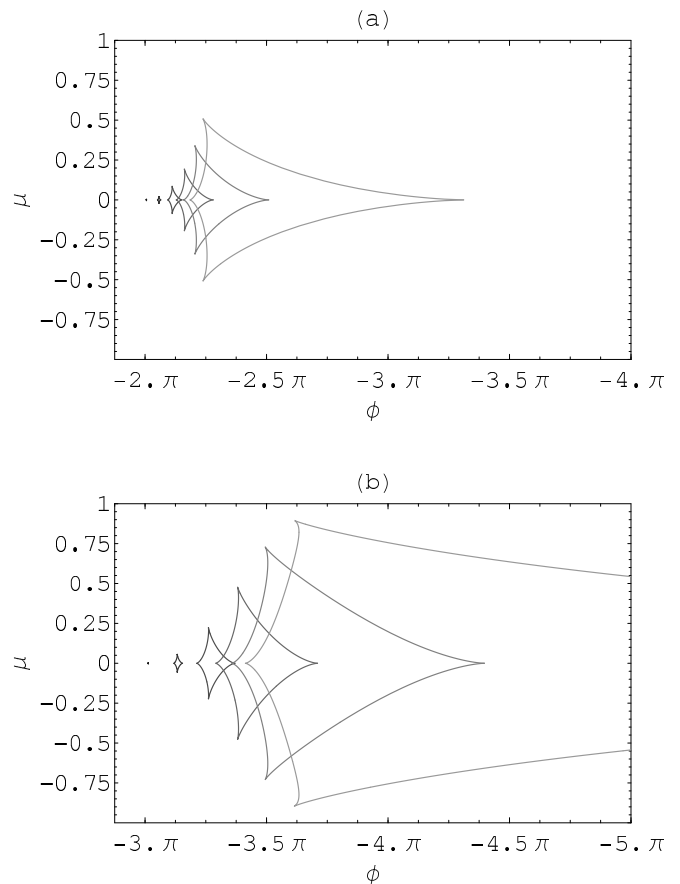


FIG. 7: Second order (a) and third order asymptotic caustics (b) for an equatorial observer  $\mu_o = 0$  and different values of the spin. From left to right,  $a = 0.02M, 0.2M, 0.4M, 0.6M, 0.8M, 0.9998M$ .

order caustic (first retro-lensing caustic) and the third order caustic (second standard lensing caustic) for different values of the spin. At very low values of  $a$ , higher order caustics are very small and only slightly displaced from the Schwarzschild positions  $\phi = -m\pi$ . As  $a$  grows, the size and the displacement of the caustics grow. At the same time, the caustics become asymmetric, with the cusp on the right (corresponding to prograde photons) more stretched than the cusp on the left (retrograde photons).

At nearly extremal spins, higher order caustics become very large but do not undergo any transitions to different shapes. This regime is particularly interesting and will be deeply investigated in the following section.

Now we turn to the dependence of the asymptotic caustics on the spin inclination with respect to the line of sight. In Fig. 8 we show some asymptotic cross-sections of the caustics for different values of the spin inclination  $\mu_o$ . The retro-lensing caustics are always centered on  $\mu_o$ , i.e., they lie at the same latitude as the observer, whereas the standard lensing caustics lie at opposite latitude. Both retro-lensing and standard lensing caustics preserve the same shift in the azimuthal direction as the

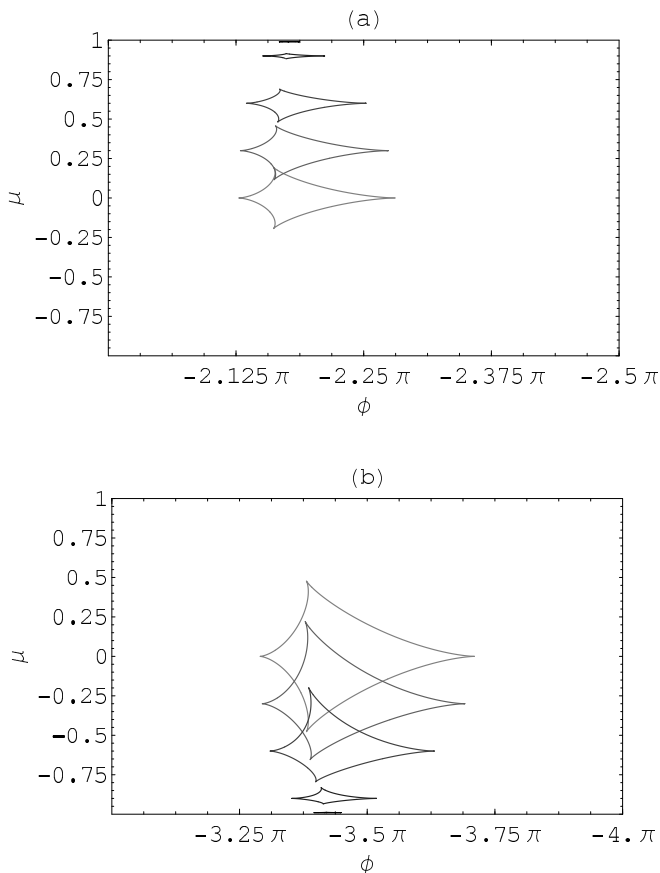


FIG. 8: Second order (a) and third order asymptotic caustics (b) generated by a Kerr black hole with spin  $a = 0.6M$  for different values of the inclination  $\mu_o = \cos \vartheta_o$ . From the center to the periphery,  $\mu_o = 0, 0.3, 0.6, 0.9, 0.99$ .

$\mu_o = 0$  caustic. Increasing  $\mu_o$  from 0 (observer on the equatorial plane) to 1 (observer on the polar axis), all higher order caustics gradually shrink to zero size. An observer on the polar axis would thus have point-like caustics on the optical axis as in the Schwarzschild case. Another interesting feature is that the caustics are slightly stretched on the side closer to the equatorial plane. This is not just an effect of the use of the projected coordinate  $\mu$  as it can be seen even in terms of the polar angle  $\vartheta$ . We must conclude that multiple images arise more easily for sources close to the equator.

In order to double-check our numerical calculations, we can compare our asymptotic caustics with some approximation schemes. The first is the one developed in Ref. [26], based on the Strong Deflection Limit. In that paper, only the intersections of the caustics with the equatorial plane have been calculated numerically. Nevertheless, a comparison with these results allows us to check the retrograde and prograde cusp positions with a completely independent calculation. The second approximation is provided by the fully analytical formulae derived in Refs. [18, 19, 20] in the Strong Deflection Limit with an expansion to second order in the black hole spin  $a$ . They

read

$$\mu_s = (-1)^m \left[ \mu_o + R_m (1 - \mu_o^2)^{3/2} \sin^3 \eta \right], \quad (11)$$

$$\phi_s = -m\pi - \Delta\phi_m + R_m \sqrt{1 - \mu_o^2} \cos^3 \eta, \quad (12)$$

where the azimuthal shift is

$$\Delta\phi_m = - \left\{ \frac{2m\pi}{3\sqrt{3}} + 2 \log \left( 2\sqrt{3} - 3 \right) + \log \left[ \frac{(2\sqrt{r_s} + \sqrt{6M + r_s})}{3\sqrt{(r_s - 2M)}} \right] \right\} a, \quad (13)$$

and the semi-amplitude of the caustic is

$$R_m = a^2 \left[ \frac{1}{18} (5m\pi + 8\sqrt{3} - 36) + \frac{(9M + 2r_s - 2\sqrt{r_s}\sqrt{6M + r_s})}{3\sqrt{3}\sqrt{r_s}\sqrt{6M + r_s}} \right]. \quad (14)$$

In the limit  $r_s \gg 2M$ , these expressions reduce to their first lines respectively.

Fig. 9 shows the dependence of the positions of the cusps of the asymptotic caustic on the black hole spin. Along with our numerical results, we have plotted the two approximations described above. We see that the Schwarzschild limit is correctly reproduced as  $a \rightarrow 0$ , since the caustics become point-like and return to the optical axis ( $-2\pi$  for the second order caustic and  $-3\pi$  for the third order caustic). As soon as we switch the spin on, the caustics are shifted clockwise (more negative  $\phi$ ) and acquire finite extension, since the prograde cusp is more shifted than the retrograde cusp.

The perturbative approximation works quite well up to  $a \simeq 0.2M$ . At higher spins, it underestimates the shift of the caustics. On the other hand, the SDL approximation without the expansion in powers of  $a$  works extremely well for the third order caustic, as the solid and dotted lines are practically indistinguishable in Fig. 9b. For the second order caustic, instead, it works quite well for the retrograde cusp but fails at moderate and high spin values for the prograde cusp. We must keep in mind that the SDL approximation is designed for high caustic orders and is just marginally applicable to the second order caustic.

Now let us come to the full development of the caustic surfaces, from very far source distances up to the horizon. In Fig. 10 we show the second order caustic tube for a rather small value of the spin ( $a = 0.2M$ ). It looks quite similar to the primary caustic. The caustic tube has astroidal cross-section and winds an infinite number of times around the horizon. However, the cross-section does not shrink to zero size at infinity, but preserves the same angular size. A 3-dimensional picture containing several caustics at the same time would not be so readable, as all caustics wind around the horizon so tightly that they would be undistinguishable. However, a picture giving the idea of how several caustics wind around the

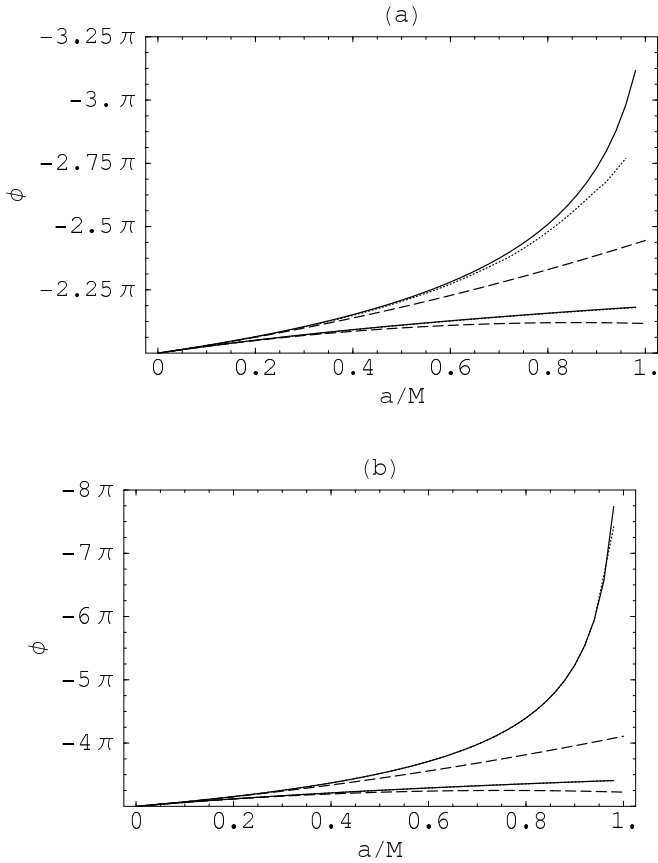


FIG. 9: Azimuthal position of the prograde and retrograde cusps of the asymptotic caustic as a function of the black hole spin. (a) Second order caustic; (b) Third order caustic. The solid lines are from numerical results in this paper, the dotted lines are the SDL approximation of Ref. [26], the dashed lines are the perturbative results of Ref. [19].

black hole is in Fig. 11, where we have represented the projection of the caustics on the equatorial plane. The radial coordinate has been replaced by the logarithmic coordinate  $\log(r_s - r_h)/2M + 11$  in order to put the “spiral arms” of the caustics in better evidence. Of course, such a representation becomes meaningless at distances less than  $r_h + 10^{-11}M$ . We have represented the primary caustic (labelled by “1”) along with higher order caustics up to the sixth order. In this way we have explicitly shown where the caustics lie with respect to the observer’s direction (labelled by “O”). In the Schwarzschild limit, all caustics reduce to a line: odd ones are on the opposite side and even ones (retro-lensing caustics) are on the same side as the observer. At  $a > 0$ , all caustics are shifted clockwise and acquire a finite extension, proportionally to their order.

Let us come to a more quantitative analysis. Fig. 12 shows the azimuthal position of the retrograde cusp as a function of the radial coordinate for the second and third order caustic. The behavior is very similar to the primary caustic, with the logarithmic divergence for  $r_s \rightarrow r_h$ . However, at large radii, the retrograde cusp does not

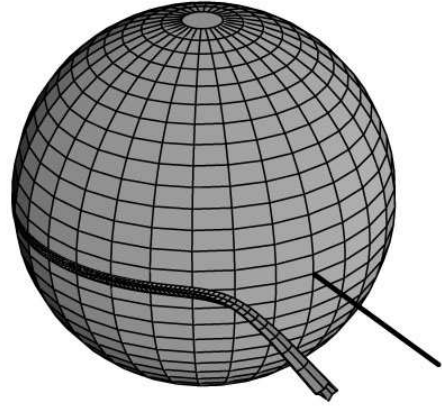


FIG. 10: The second order caustic surface for  $a = 0.2M$  and  $\mu_o = 0$ . The straight line indicates the direction towards the observer.

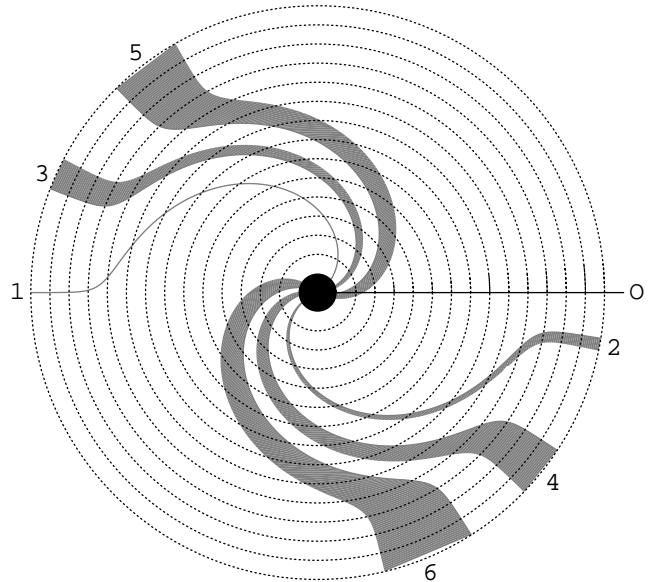


FIG. 11: A representation of the caustics on the equatorial plane in which the radial coordinate has been replaced by  $\log(r_s - r_h)/2M + 11$ . The outer circle represents the surface at  $\log(r_s - r_h)/2M = 4$ . Inner circle are in steps of 1 in such a logarithmic coordinate. The observer is in the direction labelled by “O” on the equatorial plane. The number at the end of each caustic represents the respective caustic order. Here the spin is  $a = 0.2M$  with the black hole rotating counterclockwise.

settle to the Schwarzschild position  $-m\pi$ , but a finite shift remains. In Fig. 13 we plot the size of the caustics (estimated as the distance between the prograde and the retrograde cusp) as a function of the radial coordinate. Indeed, the size of the caustics tends to two different constants at large and small radii. This behavior has already been noted for small  $a$  caustics in Ref. [20].

We conclude this section by a picture representing the relative error in the prediction of the position and size of

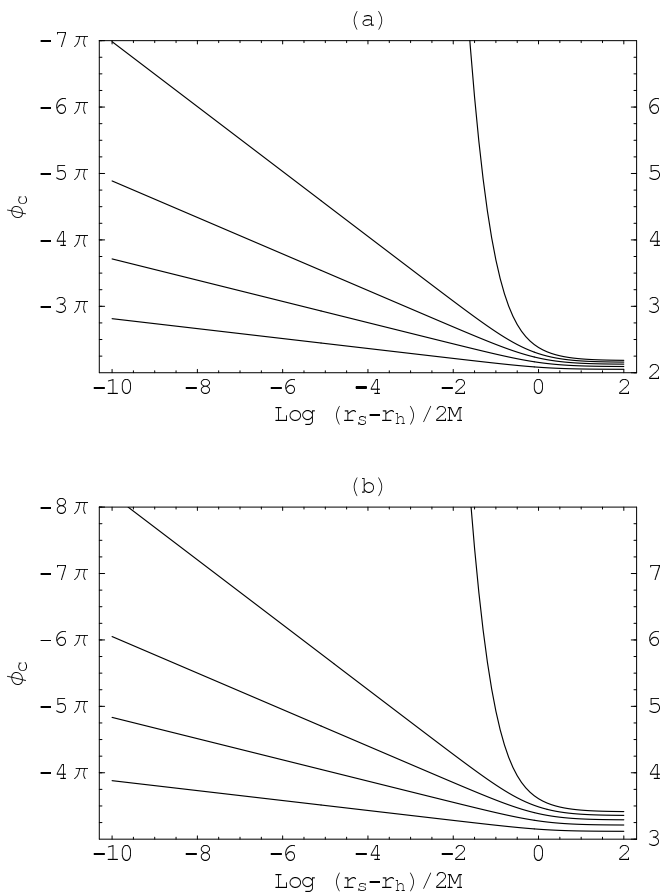


FIG. 12: Position of the retrograde cusp for the second order (a) and the third order (b) caustics, as a function of the radial coordinate. In both figures, from bottom to top, the curves are for  $a = 0.2M, 0.4M, 0.6M, 0.8M, 0.9998M$ .

the caustics by the perturbative formulae (13) and (14). In Fig. 14 we can see that the error decreases exponentially with the caustic order  $m$ , as predicted by the SDL approximation. However, a residual error remains because of the expansion in powers of  $a$ . In any case, for the value  $a = 0.02M$  used in this plot, the error is at most of 3% for the second order caustic at large distances. Therefore, the SDL approximation works amazingly well at all radial distances, reproducing the logarithmic spiralling perfectly.

## V. CAUSTICS OF EXTREMAL KERR BLACK HOLES

As shown in the previous sections, higher order caustics become very large at high values of the spin. Since there are several indications that nearly extremal spinning black holes may be not uncommon in the universe, it is particularly important to focus on the caustic structure of this particular limiting species of Kerr black holes.

First, we show the asymptotic cross-sections at large

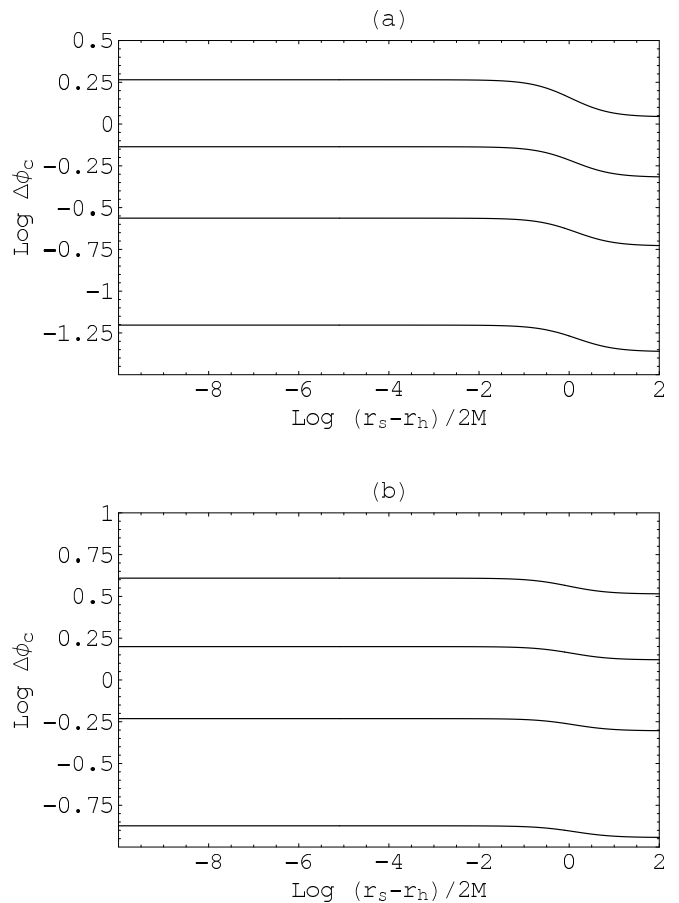


FIG. 13: Size of the second order (a) and the third order (b) caustics, as a function of the radial coordinate. In both figures, from bottom to top, the curves are for  $a = 0.2M, 0.4M, 0.6M, 0.8M$ .

source distances for several caustic orders. Apart from the second order caustic, all higher order caustics extend for more than a complete loop around the black hole. The left (retrograde) cusp is shifted clockwise from the Schwarzschild position linearly with the caustic order  $m$ , following the law

$$\phi_l = -3.86m + 0.87. \quad (15)$$

On the contrary, the right (prograde) cusp is shifted exponentially with  $m$ , following the law

$$\phi_r = -1.05m - 0.36 \exp(1.57m). \quad (16)$$

Caustics overlap each other without any interference, as they correspond to trajectories with different numbers of inversion points in the polar motion, which live in different regions of the  $(\psi, \eta)$  space. Also the extension in latitude increases, with the northern and southern cusps gradually approaching the poles.

The reader may wonder about the physical consequences of having caustics extending for more than  $2\pi$  in azimuth. In Fig. 16 we plot the third order caustic

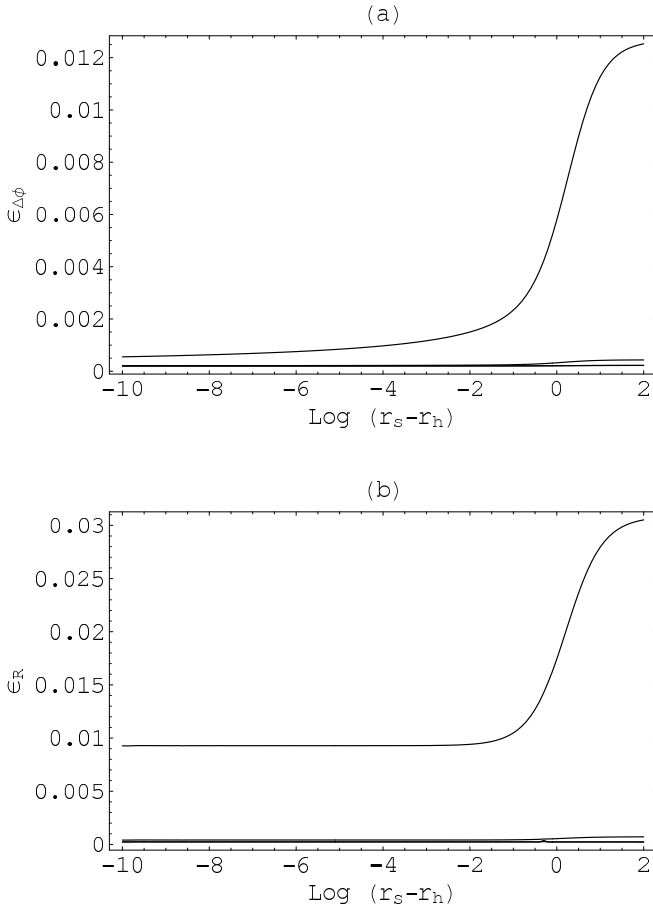


FIG. 14: Relative error of the perturbative approximation given by Eqs. (13) and (14) as function of the radial coordinate. (a) Error in the shift of the caustic (b) Error in the size of the caustic. Curves are for caustic orders  $m = 2, 3, 4$  from top to bottom.  $a = 0.02M$ ,  $\mu_o = 0$ .

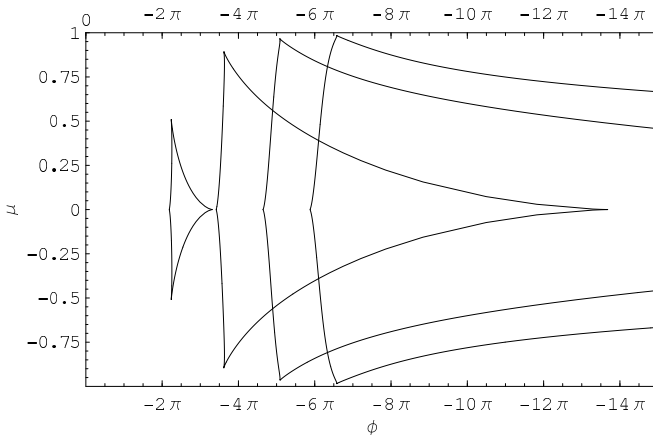


FIG. 15: Asymptotic caustics of an extremal Kerr black hole for an equatorial observer. From left to right the caustic order is  $m = 2, 3, 4, 5$ .

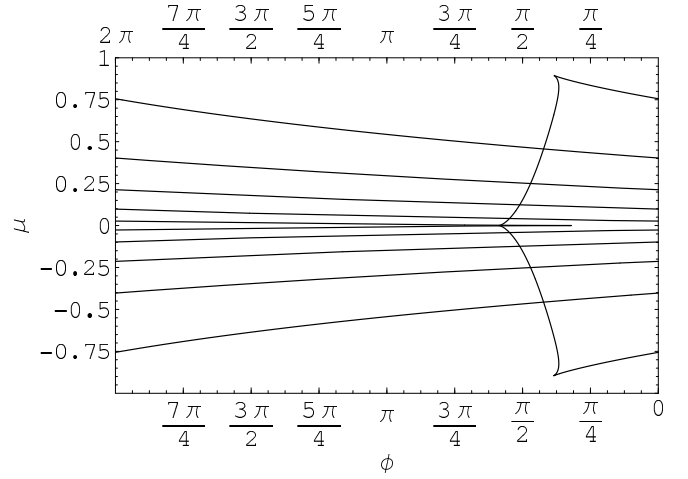


FIG. 16: Third order asymptotic caustic of an extremal Kerr black hole for an equatorial observer in the  $\phi$ - $\mu$  plane. In this plot, we have taken into account the fact that the azimuthal coordinate is periodic with period  $2\pi$ .

reporting all points in the physical interval  $0 \leq \phi < 2\pi$ . In this way, the caustic appears to exit from the right side and re-enter from the left side for five times before it ends in the prograde cusp. Suppose to have a source on the same side of the observer ( $\phi_s \simeq 0$ ) and close enough to the northern pole ( $\mu_s \simeq 1$ ) to be outside of the caustic surface. In this situation, there are only two images formed by photons with three inversions in the polar motion. If we move the source down, by decreasing  $\mu_s$ , the source meets the caustic for the first time. At this point, two new images appear, as we know from gravitational lensing theory. Their initial position on the critical curve is the one that corresponds to the caustic point where the source crosses the caustic. However, if we continue to move the source down, at some point we meet the caustic for the second time. Two new images appear in a different position on the critical curve. In particular, these new images are still formed by photons with three inversion points in the polar motion but they perform one more loop in the azimuthal motion before reaching the observer with respect to the previous pair. If we continue to decrease  $\mu_s$ , we can cross the caustic 4 more times, including the final cusp crossing. Therefore, for an extremal Kerr black hole, we can have up to 14 images with three inversion points in the polar motion.

The number of times a particular caustic can be crossed is simply given by the number of azimuthal loops spanned by the caustic plus one. With the empirical formulae (15) and (16), we can estimate that a caustic of order  $m$  may generate up to

$$n = [0.36 \exp(1.57m) - 2.82m + 0.87] \quad (17)$$

new pairs of images. In practice, for a source very close to the pole, the number of images with  $m$  inversions in the polar motion will always be the minimal one, i.e. 2. On the other hand, for a source close to the equatorial

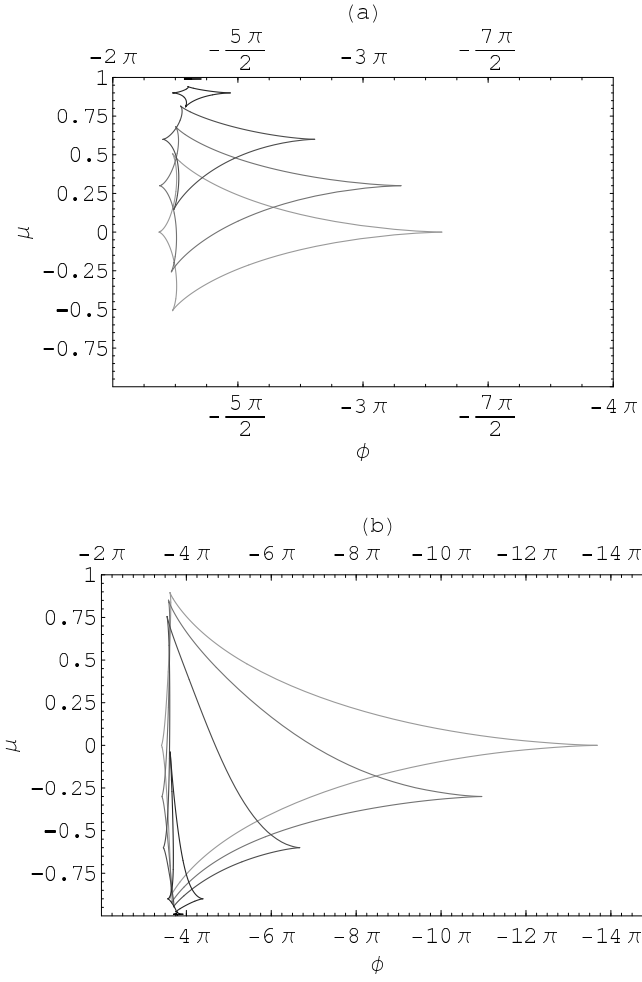


FIG. 17: Second order (a) and third order (b) asymptotic caustics of an extremal Kerr black hole for different positions of the observer. From the center to the periphery the caustics are drawn for  $\mu_o = 0, 0.3, 0.6, 0.9, 0.99$ .

plane, the number of images will always be very close to the maximal one  $2(n + 1)$ . It is interesting to connect this result with the exponential decrease in the magnification of higher order images with the caustic order. From one side we have an exponential increase of the number of images. From the other side we have an exponential decrease in the magnification factor of each image. However, even if we have not calculated the details of the magnification, we can expect that the decrease in the magnification dominates on the increase in the number of images, in such a way that the total flux in the images of order  $m$  still decreases exponentially with the caustic order. Finally, we also note that, apart from the first pair of additional images, all images created by repeated caustic crossings occur in a region close to the stretched prograde cusp. Therefore, all these additional images will appear to the observer on the left side of the black hole.

As for the dependence of the caustics on the spin inclination on the line of sight, we have plotted several second order and third order caustics in Fig. 17. As in Fig. 8,

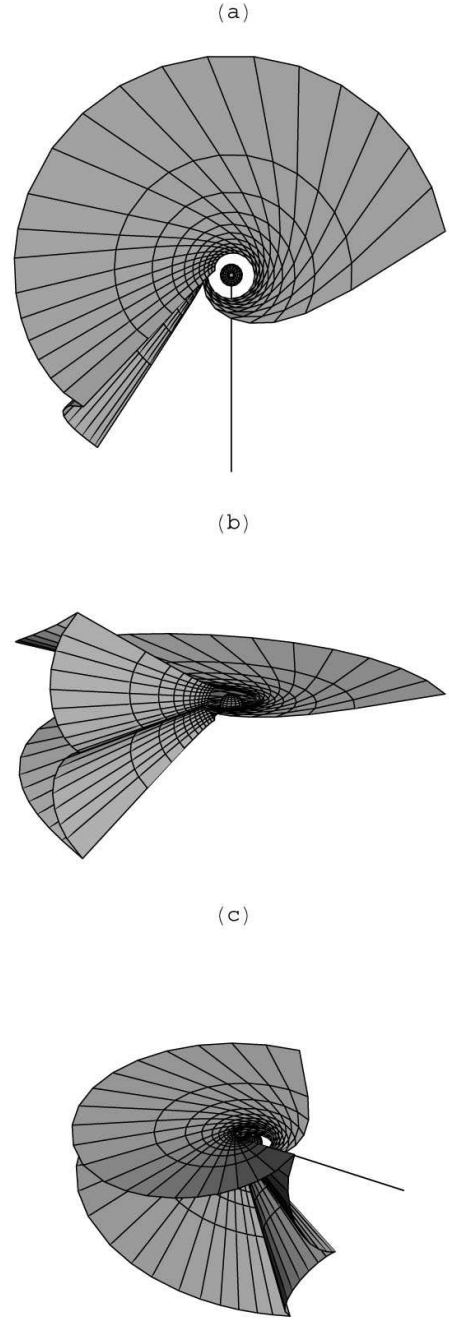


FIG. 18: 3-dimensional pictures of the second order caustic surface of an extremal Kerr black hole for an observer on the equatorial plane. The surface has been plotted for radial distances in the range  $[2.2M, 20M]$ . (a) View from the north pole. (b) View from the observer side, lifted by  $10^\circ$  above the equator. (c) View from the left side. The straight line in (a) and (c) points towards the observer.

the caustics keep the same azimuthal shift for their central region while their size decreases with increasing  $\mu_o$ . Even if the  $\mu_o = 0$  caustics extend for several azimuthal loops, by increasing  $\mu_o$  up to  $\mu_o = 1$ , all caustics shrink to a point. Furthermore, we can see in particular from Fig. 17b that the caustics maintain their extension in lat-

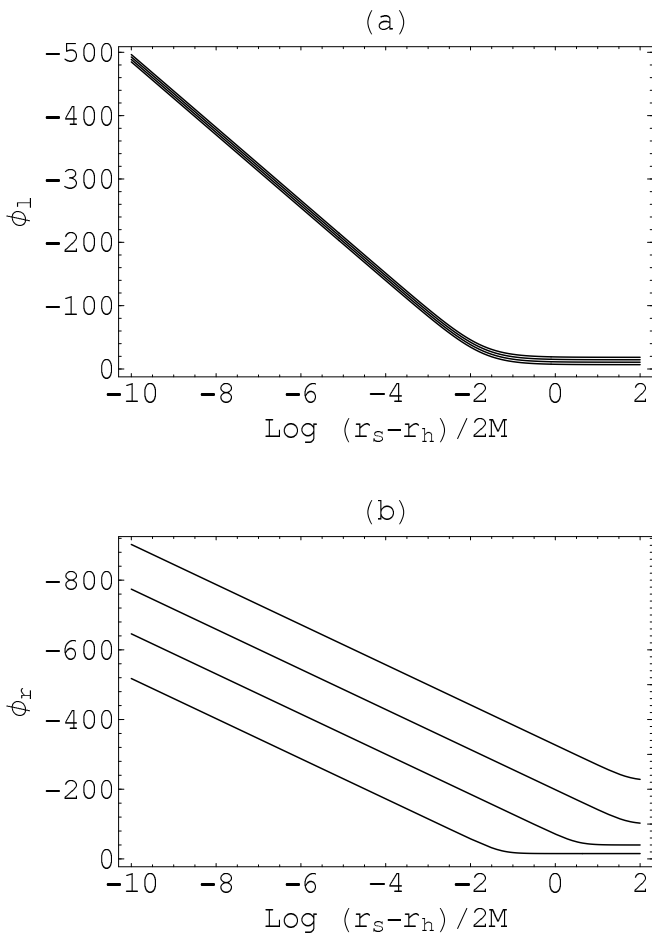


FIG. 19: Azimuthal position of the retrograde cusp (a) and prograde cusp (b) as a function of the logarithm of the distance from the event horizon. From bottom to top, the curves are for caustic order  $m = 2, 3, 4, 5$ .

itude until the azimuthal stretch is reduced to less than one loop. Only then, the latitudinal size starts to decrease significantly. As a consequence, since the left and right cusps are always at  $\mu = \pm\mu_o$ , we have a considerable asymmetry between the side of the caustic towards the pole and the side towards the equator, which remains much larger.

After the study of the asymptotic cross-section of the caustic surfaces, it is time to examine the full development of the caustics of an extremal Kerr black hole. As it can be deduced from the extension of the asymptotic cross-sections, the caustic surfaces become so wide that they no longer resemble a tube. They assume an almost disk-like shape with the thickness increasing with the distance from the black hole. Some 3-dimensional pictures of the second order caustic are shown in Fig. 18 with different points of view. The caustic has been calculated for an observer on the equatorial plane (whose direction is indicated by the straight line). One can appreciate the half-disk shape which winds around the black hole more and more. The retrograde cusp is the equatorial

cusps on the left side, which also enjoys the wider latitudinal extension. The prograde cusp is on the right side, where the caustic has a spiky cross-section. The prograde cusp winds around the black hole much more quickly than the retrograde cusp, at least initially. It can be easily imagined that the pictures of even higher order caustic surfaces, which spread over several loops around the black hole, are very difficult to show in a clear way. The caustic surface self-intersects several times.

Finally, we plot the position of the retrograde and prograde cusps in Fig. 19. We can see that both retrograde and prograde cusps wind around the black hole following the usual logarithmic law  $\phi \sim c \log(r_s/r_h - 1)$ . However, the prograde cusps start to follow the logarithmic law at much larger distances than the retrograde cusps. This means that the caustic has a very large increase from the asymptotic size at large radial distances to the final size at distances very close to the black hole. The slope of the logarithmic laws is the same for all prograde and retrograde cusps and amounts to  $c = 57.55$ , which means that each time we decrease the distance from the horizon by a factor 10, the caustic makes 9.16 turns around the black hole.

## VI. CRITICAL CURVES

As stated in Section II, once we find a critical point of the lens mapping in the  $(\psi, \eta)$  space, we can easily determine the corresponding critical point in the observer's sky, spanned by the angular coordinates  $(\theta_1, \theta_2)$ . As  $\eta$  varies from  $-\pi$  to  $\pi$ , the critical points describe a closed curve around the black hole. Therefore, for each caustic order  $m$ , for a given source distance  $r_s$ , we have a distinct critical curve in the observer's sky. In particular, the primary critical curve of order  $m = 1$  is the classical Einstein ring. If a source at distance  $r_s$  lies on the primary caustic tube and is large enough that a complete cross-section of the caustic tube lies inside the source, then the observer will see the primary image and the secondary image merged together to cover the whole Einstein ring. Since higher order caustics have a greater extension, the case that a source intercepts a complete cross-section of the caustic tube can only occur for sufficiently low spins or very large sources. Therefore, it is much more difficult to have a complete Einstein ring of higher order. Nevertheless, critical curves are the loci where additional pairs of images appear or disappear when a caustic crossing occurs. Since such images are maximally magnified during the process of creation or destruction, it is important to study critical curves because they indicate the places where higher order images are most likely to be detected. However, the average radius of a critical curve depends on the source distance. This is particularly evident for the primary critical curve, whose average radius at large source distances scales as the Einstein angle  $\theta_E = \sqrt{4Mr_s/r_o(r_o + r_s)}$ . Higher order critical curves tend to an asymptotic shape for large source distances,

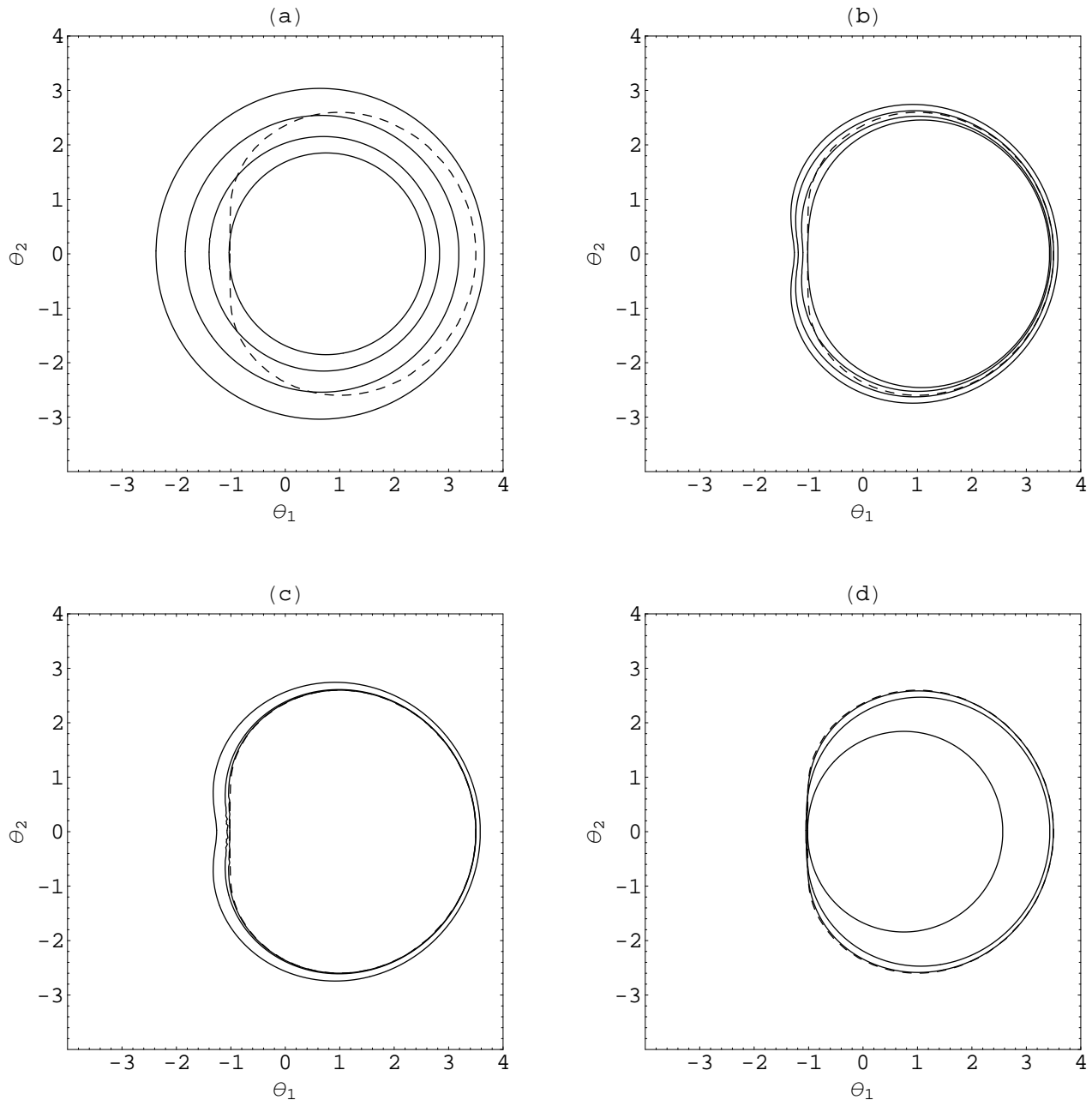


FIG. 20: Critical curves for a Kerr black hole with spin  $a = 0.9998M$  and an equatorial observer. The coordinates  $(\theta_1, \theta_2)$  in the observer's sky are in units of  $2M/r_o$ . (a) Primary critical curve for various source distances: starting from the outside,  $r_s = 5M, 3M, 1.8M, 1.1M$ . (b) Second order critical curve for various source distances: starting from the outside,  $r_s = \infty, 4.2M, 1.6M, 1.1M$ . (c) Critical curves of order  $m = 2, 3, 4$  for a source at infinity. (d) Critical curves of order  $m = 1, 2, 3$  for a source at  $r_s = 1.1M$ . The shadow border is represented by the dashed curve.

whereas they become smaller for smaller source distances. Typically, higher order critical curves are slightly larger than the shadow of the black hole, but when the source is closer than the unstable photon orbits, the critical curves appear entirely inside the shadow of the black hole.

In Fig. 20 we show some critical curves for a nearly

extremal Kerr black hole and an equatorial observer. As well-known [2], the shadow is shifted to the right (retrograde side) with respect to the black hole position, with the left (prograde) side more flattened.

In Fig. 20a we show the primary critical curve for various source distances. If the source is far from the black

hole, the critical curve is also far from the shadow. If the source is closer to the black hole, the critical curve shrinks gradually and finally enters the shadow when the source is closer to the black hole. Note that the critical curve enters the shadow from the retrograde side first, because the retrograde unstable orbit lies at a larger radius. The prograde unstable orbit is closer to the horizon and therefore the critical curve stays outside the shadow on the prograde side until the source becomes very close to the horizon. We can also note that the primary critical curve maintains its nearly circular shape at all source distances.

Higher order critical curves, instead, follow the shape of the shadow more closely. In Fig. 20b we show the second order critical curve for various source distances. At very large source distances each critical curve tends to a fixed asymptotic curve at finite distance from the shadow. As the source distance is decreased, the critical curve shrinks and finally enters the shadow. Note that higher order critical curves have a small concavity on the prograde side, which disappears when the source is closer to the black hole.

In Fig. 20c we show the critical curves of order  $m = 2, 3, 4$  altogether for a source at infinity. All critical curves are outside the shadow with higher order ones closer to the shadow. In Fig. 20d we show the critical curves of order  $m = 1, 2, 3$  for a source at  $r_s = 1.1M$  i.e. very close to the horizon. In this case the primary curve is the most internal one, with the higher order ones gradually closer to the shadow.

Finally, the dependence of the critical curves on the spin inclination closely follows the dependence of the shadow, which becomes more and more circular and symmetric as the observer's latitude increases.

## VII. CONCLUSIONS

In all applications of gravitational lensing, the study of critical curves and caustics of specific lens models has always represented a fundamental step in the comprehension of the whole phenomenology. As it can be easily imagined, the derivation of caustic surfaces in a full general relativistic context is much more involved than in classical lens models analyzed under the weak deflection paradigm. The simplest general relativistic lens is the Schwarzschild black hole. In this model, however, the caustics are degenerate and are therefore trivially tractable. The first general relativistic lens with a non-trivial caustic structure is the Kerr black hole. Going beyond the results of previous works, focused on particular limits of the caustics [15, 16, 18, 19, 20], this paper contains a complete investigation of the full caustic structure of the Kerr metric. This represents a considerable step forward for gravitational lensing phenomenology in full General Relativity.

In summary, we have shown 3-dimensional pictures of the primary and higher order caustic surfaces. We have

analyzed the dependence of the cross-sections of the caustic surfaces on the source distance, the black hole spin, the spin inclination and the caustic order. We have shown that the caustic surfaces always wind an infinite number of times around the horizon following a logarithmic law. The size of the caustics always remains finite in the whole parameter space and there are no transitions to different kinds of caustic singularities in the lens mapping. For extremal spin values, the size of higher order caustics increases exponentially with the caustic order. This implies that the number of higher order images also grows exponentially, as the same caustic can be crossed an exponential number of times. We have compared our results with previous analytical and numerical approximations, finding perfect agreement in the respective limits of validity of the approximations. We have also shown some critical curves in the observer's sky, focusing on their dependence on the source distance.

In addition, the code developed in this paper for the calculation of the caustics is particularly well-suited for the study of higher order images, as being inspired by the Strong Deflection Limit methodology. An interesting future development of this code might be the implementation of an efficient resolution algorithm of the Kerr lens equation including higher order images.

Besides the purely theoretical interest of the analysis presented in this paper, we can easily imagine that the knowledge of the complete caustic structure of the Kerr black hole in all ranges of parameters will stand as an extremely helpful guide in future astrophysical applications involving very strong light bending by the gravitational field of spinning black holes.

## Acknowledgments

The author thanks Gaetano Scarpetta and Mauro Sereno for useful comments on the manuscript. We acknowledge support for this work by MIUR through PRIN 2006 Protocol 2006023491.003, by research funds of Agenzia Spaziale Italiana, and by research funds of Salerno University.

## APPENDIX A: FROM THE GEODESICS EQUATION TO THE LENS MAPPING

In this appendix, we describe all the steps of the calculation of the caustics in Kerr spacetime. Section A 1 recalls the basic facts about Kerr geodesics. Section A 2 discusses the unstable photon orbits and the choice of good variables for numerical integration. Section A 3 deals with angular integrals, Section A 4 with radial integrals. Section A 5 introduces the  $\psi$  variable and shows the lens mapping explicitly. Finally, Section A 6 discusses details on the numerical implementation of the strategy for searching critical points and drawing caustic surfaces.

## 1. Basics of Kerr geodesics

Thanks to the separability of the Hamilton-Jacobi equation [27], the geodesic motion for a massless particle is described by two integral equations

$$\pm \int \frac{dr}{\sqrt{R}} = \pm \int \frac{d\vartheta}{\sqrt{\Theta}} \quad (\text{A1})$$

$$\begin{aligned} \phi_f - \phi_i = & a \int \frac{r^2 + a^2 - aJ}{\Delta\sqrt{R}} dx - a \int \frac{dx}{\sqrt{R}} \\ & + J \int \frac{\csc^2 \vartheta}{\sqrt{\Theta}} d\vartheta, \end{aligned} \quad (\text{A2})$$

where

$$\Theta = Q + a^2 \cos^2 \vartheta - J^2 \cot^2 \vartheta \quad (\text{A3})$$

$$\begin{aligned} R = & r^4 + (a^2 - J^2 - Q)r^2 + 2Mr(Q + (J - a)^2) \\ & - a^2 Q, \end{aligned} \quad (\text{A4})$$

$J$  and  $Q$  are two constants of motion. The first can be identified with the projection of the angular momentum of the particle on the spin axis and the second is related to the square of the total angular momentum. The double signs before the integrals are chosen in such a way that all pieces of the integrals between two consecutive inversion points are summed with a positive sign.

A photon reaching the observer with constants of motion  $J$  and  $Q$  will then be detected by the observer at angular coordinates [2]

$$\theta_1 = -\frac{J}{r_o \sqrt{1 - \mu_o^2}}, \quad (\text{A5})$$

$$\theta_2 = \pm r_o^{-1} \sqrt{Q + \mu_o^2 \left( a^2 - \frac{J^2}{1 - \mu_o^2} \right)}. \quad (\text{A6})$$

Only an indetermination on the sign of  $\theta_2$  remains.

Conversely, the constants of motion of a photon reaching the observer from angles  $(\theta_1, \theta_2)$  are found by inverting Eqs. (A5)-(A6)

$$J = -\theta_1 r_o \sqrt{1 - \mu_o^2}, \quad (\text{A7})$$

$$Q = \theta_2^2 r_o^2 + \mu_o^2 (\theta_1^2 r_o^2 - a^2). \quad (\text{A8})$$

## 2. Choosing good labels for photon trajectories

All photon trajectories ending at the observer can be completely specified by assigning proper values to the constants of motion  $J$  and  $Q$ . Equivalently, one can specify the coordinates in the observer sky  $\theta_1$  and  $\theta_2$ . However, in order to keep numerical errors low, we may need to find new labels for the photon trajectories. In the case of the Kerr metric, the most challenging geodesics are those approaching the unstable photon orbit. We have found that using variables inspired by the Strong

Deflection Limit (SDL) technique [19] proves very convenient, opening the way to a reliable description of higher order caustics. Therefore, in this subsection we recall the definition of the SDL parameters  $\delta$  and  $\epsilon$ , and introduce the variable  $\eta$  which replaces the  $\xi$  of Ref. [19].

The inversion points in the radial motion are obtained by solving Eq.  $R = 0$ . Photons reaching an observer at infinity can have one or zero radial inversion points. If  $\partial R/\partial r = 0$  is satisfied at the same time with  $R = 0$  for some value  $r = r_m$ , then the photon remains at radial coordinate  $r_m$  forever. However, small perturbations would make the photon fall into the black hole or escape to infinity, because the circular photon orbits around Kerr black holes are unstable. The unstable photon orbits are characterized by particular values of the constants of motion  $J$  and  $Q$ . In order to find them, we can solve equations  $R = 0$  and  $\partial R/\partial r = 0$  for  $J$  and  $Q$  as functions of  $r = r_m$ . As  $r_m$  varies,  $J$  and  $Q$  describe a locus in the  $(J, Q)$  space, corresponding to all possible unstable photon orbits. Explicitly, this locus is given by [2]

$$J_m(r_m) = \frac{(3M - r_m)r_m^2 - a^2(r_m + M)}{a(r_m - M)} \quad (\text{A9})$$

$$Q_m(r_m) = \frac{r_m^3 [4a^2 M - r_m(r_m - 3M)^2]}{a^2(r_m - M)^2}. \quad (\text{A10})$$

A photon orbiting at  $r_m$  is thus characterized by constants  $J_m(r_m)$  and  $Q_m(r_m)$ . The allowed values of  $r_m$  are those keeping  $Q$  positive. By perturbing the unstable orbit, we can make the photon escape and reach a distant observer. In this case, plugging Eqs. (A9)-(A10) into Eqs. (A5)-(A6), one finds that the escaped photon is detected at position

$$\theta_{1,m}(r_m) = \frac{r_m^2(r_m - 3M) + a^2(r_m + M)}{r_o a(r_m - M) \sqrt{1 - \mu_o^2}} \quad (\text{A11})$$

$$\theta_{2,m}(r_m) = \pm \frac{\sqrt{\Lambda(r_m)}}{M r_o a(r_m - M) \sqrt{1 - \mu_o^2}} \quad (\text{A12})$$

$$\begin{aligned} \Lambda(r_m) = & r_m^3 [4M a^2 - r_m(r_m - 3M)^2] \\ & - 2a^2 r_m (2a^2 M - 3M 2r_m + r_m^3) \mu_o^2 \\ & - a^4 (r_m - M)^2 \mu_o^4. \end{aligned} \quad (\text{A13})$$

Not all perturbed photons can reach an observer out of the equatorial plane. Only those photons with  $r_m$  such that  $\Lambda(r_m) > 0$  can be detected. Solving Eq.  $\Lambda(r_m) = 0$  numerically, we can find the two extrema of the allowed interval for  $r_m$  for any given values of the parameters  $a$  and  $\mu_o$ . We shall indicate these two extrema by  $r_+$  and  $r_-$ .

Letting  $r_m$  vary between  $r_+$  and  $r_-$  in Eqs. (A11) and (A12) and allowing both signs for  $\theta_2$ , we obtain a closed curve in the observer's sky, which is usually referred to as the border of the "shadow" of the black hole, because the radiation deflected from the black hole would appear outside this closed curve. Some shadows borders for different values of  $a$  are shown in Fig. 1. When the observer lies on the equatorial plane ( $\mu_o = 0$ ),  $r_+$  coincides with

the radius of the unstable photon orbit for equatorial prograde photons, whereas  $r_-$  becomes the radius of the unstable photon orbit for equatorial retrograde photons, which is typically larger. Increasing the inclination,  $r_+$  and  $r_-$  approach each other until they coincide when the observer lies at the pole of the black hole ( $\mu_o = 1$ ).

As  $r_+$  and  $r_-$  depend on the spin and the inclination, it is convenient to introduce the variable  $\eta$ , related to  $r_m$  by

$$r_m = \frac{1}{2} [r_+(1 - \cos \eta) + r_-(1 + \cos \eta)]. \quad (\text{A14})$$

As  $\eta$  varies from 0 to  $\pi$ ,  $r_m$  varies from  $r_-$  to  $r_+$ . If we replace the double sign in Eq. (A12) by  $\text{sign}[\eta]$ , we can get the whole shadow border at once, by varying  $\eta$  in the range  $[-\pi, \pi]$ .

As anticipated in Section II,  $\eta$  works as an angular coordinate:  $\eta = 0$  corresponds to retrograde photons, appearing on the right of the black hole;  $\eta = \pi/2$  corresponds to photons on nearly polar orbits, reaching the observer from above the black hole;  $\eta = \pi$  corresponds to prograde photons, detected on the left of the black hole.

In addition, we introduce the new variable  $\epsilon$  by the relations

$$\theta_1 = \theta_{1,m}(\eta)(1 + \epsilon) \quad (\text{A15})$$

$$\theta_2 = \theta_{2,m}(\eta)(1 + \epsilon). \quad (\text{A16})$$

As  $\epsilon$  varies in the range  $[-1, +\infty)$  and  $\eta$  in  $[-\pi, \pi]$ ,  $\theta_1$  and  $\theta_2$  span the whole observer sky. This construction is very close to that presented in Ref. [19], though here we make no expansion in powers of  $a$ . The variables  $\eta$  and  $\epsilon$  can be used to label geodesics ending at the observer and are particularly well-suited for numerical calculations. The corresponding values of the constants of motion  $J$  and  $Q$  can be found by plugging Eqs. (A15) and (A16) into Eqs. (A7) and (A8).

When  $\epsilon > 0$ , Eq.  $R = 0$  admits a non-degenerate inversion point  $r_*$ , whose expression can be written as

$$r_* = r_m(1 + \delta). \quad (\text{A17})$$

$\delta$  is a function of  $\epsilon$  and  $\eta$ . It can be found by solving Eq.  $R = 0$  numerically for given values of  $\epsilon$ ,  $\eta$  and the parameters  $a$  and  $\mu_o$ . For small values of  $\epsilon$ , we have  $\delta \sim \sqrt{\epsilon}$ . However, for low values of the inclination  $\mu_o$  and for high values of the spin, prograde photons ( $\eta \simeq \pi$ ) tend to satisfy a linear relation of the type  $\delta \sim \epsilon$ . However,  $\delta$  is not an observable and these relations are specific of Boyer-Lindquist coordinates.

### 3. Angular integrals

Eqs. (A1) and (A2) contain integrals on the polar angle  $\vartheta$ . Performing the transformation  $\cos \vartheta = \mu$ , they

become

$$J_1 = \pm \int \frac{1}{\sqrt{\Theta_\mu}} d\mu \quad (\text{A18})$$

$$J_2 = \pm \int \frac{1}{(1 - \mu^2)\sqrt{\Theta_\mu}} d\mu, \quad (\text{A19})$$

where

$$\Theta_\mu = a^2(\mu_-^2 + \mu^2)(\mu_+^2 - \mu^2) \quad (\text{A20})$$

$$\mu_\pm^2 = \frac{\sqrt{b_{JQ}^2 + 4a^2Q} \pm b_{JQ}}{2a^2} \quad (\text{A21})$$

$$b_{JQ} = a^2 - J^2 - Q. \quad (\text{A22})$$

The integration extrema are the source and observer polar coordinates  $\mu_s$  and  $\mu_o$ . However, for each inversion in the polar motion, we must split the integration domain and change sign.

The final result can be expressed in terms of elliptic integrals of the first and third kind

$$J_1(\mu_s, \epsilon, \eta) = \frac{1}{a\mu_-} [-\text{sign}[\eta]F(\lambda_o, k) + (-1)^m \text{sign}[\eta]F(\lambda_s, k) + 2mK(k)] \quad (\text{A23})$$

$$J_2(\mu_s, \epsilon, \eta) = \frac{1}{a\mu_-} [-\text{sign}[\eta]\Pi(\mu_+^2, \lambda_o, k) + (-1)^m \text{sign}[\eta]\Pi(\mu_+^2, \lambda_s, k) + 2m\Pi(\mu_+^2, k)] \quad (\text{A24})$$

$$\lambda_s = \arcsin \frac{\mu_s}{\mu_+} \quad (\text{A25})$$

$$\lambda_o = \arcsin \frac{\mu_o}{\mu_+} \quad (\text{A26})$$

$$k = -\frac{\mu_+^2}{\mu_-^2}, \quad (\text{A27})$$

where  $m$  is the number of inversions in the polar motion, and the  $\text{sign}[\eta]$  takes into account the fact that for positive  $\eta$  the observer is reached from above and for negative  $\eta$  is reached from below. We recall the definitions of the elliptic integrals

$$F(\lambda, k) = \int_0^\lambda \frac{d\vartheta}{\sqrt{1 - k \sin^2 \vartheta}} \quad (\text{A28})$$

$$K(k) = F(\pi/2, k) \quad (\text{A29})$$

$$\Pi(n, \lambda, k) = \int_0^\lambda \frac{d\vartheta}{(1 - n \sin^2 \vartheta)\sqrt{1 - k \sin^2 \vartheta}} \quad (\text{A30})$$

$$\Pi(n, k) = \Pi(n, \pi/2, k). \quad (\text{A31})$$

Besides depending on the source polar coordinate  $\mu_s$ , the functions  $J_1$  and  $J_2$  also depend on  $\epsilon$  (weakly) and  $\eta$  through the constants of motion  $J$  and  $Q$ , appearing in the expressions of  $\mu_+$  and  $\mu_-$ .

#### 4. Radial integrals

The geodesics equations (A1) and (A2) also contain two integrals on the radial coordinate

$$I_1 = \int \frac{dx}{\sqrt{R}} \quad (\text{A32})$$

$$I_2 = \int \frac{dx}{\sqrt{R}} \int \frac{r^2 + a^2 - aJ}{\Delta\sqrt{R}} dx. \quad (\text{A33})$$

These integrals depend on the labels  $(\epsilon, \eta)$  identifying the geodesic through  $J$  and  $Q$ .

The photon might be emitted from the source either outward or inward. We must therefore distinguish these two cases and solve the integrals accordingly.

If the photon is emitted in the outward direction, there is no inversion point and the integrations are carried out in the domain  $[r_s, \infty)$ . For numerical reasons, it is convenient to change the integration variable to  $z$ , defined by

$$r = \frac{r_m}{1-z}. \quad (\text{A34})$$

Then the integration range becomes  $[1 - r_m/r_s, 1]$ . In this case, the integrand is sharply peaked at  $z = 0$  [20].

If the photon is emitted inward, it must have an inversion point  $r_*$  somewhere between  $r_m$  and  $r_s$  in order to come back and reach a distant observer. Therefore, this case is relevant for lensing only if  $\epsilon > 0$  and  $r_s > r_m$ . The radial integrals are split in two pieces: the approach piece, with extrema  $[r_*, r_s]$ , and the escape piece, with extrema  $[r_*, \infty)$ . The two pieces are conveniently calculated using the variable

$$r = \frac{r_*}{1-z}, \quad (\text{A35})$$

which maps the integration domains to the finite intervals  $[0, 1 - r_*/r_s]$  and  $[0, 1]$  respectively. In this case the integrand diverges at  $z = 0$ , but the result of the integration is finite for any value of  $\epsilon > 0$ . As  $\epsilon \rightarrow 0$ , the integrals diverge logarithmically, except for prograde orbits at high values of the spin, for which the integrals diverge as  $\epsilon^{-1}$ .

For a given source at  $r_s > r_m$ , there exists a maximum value for  $\epsilon$  (we call it  $\epsilon_{max}$ ) such that  $R$  is positive only for  $\epsilon < \epsilon_{max}$ . When  $\epsilon = \epsilon_{max}$ ,  $r_s$  becomes a solution of the equation  $R = 0$  and thus coincides with the inversion point  $r_*$ .

Summing up, the functions  $I_1(\epsilon, \eta)$  and  $I_2(\epsilon, \eta)$  have two branches if  $r_s > r_m$ : one corresponding to photons emitted outward, which exists for  $\epsilon$  in  $[-1, \epsilon_{max}]$ , and the other corresponding to photons emitted inward, existing for  $\epsilon$  in  $(0, \epsilon_{max}]$ . The two branches nicely join at  $\epsilon_{max}$ . If  $r_s < r_m$ , only the outward branch exists for  $\epsilon$  in  $[-1, 0)$ .

#### 5. Lens mapping

At this point, we introduce a new variable  $\psi$ , which considerably simplifies numerical calculations and as-

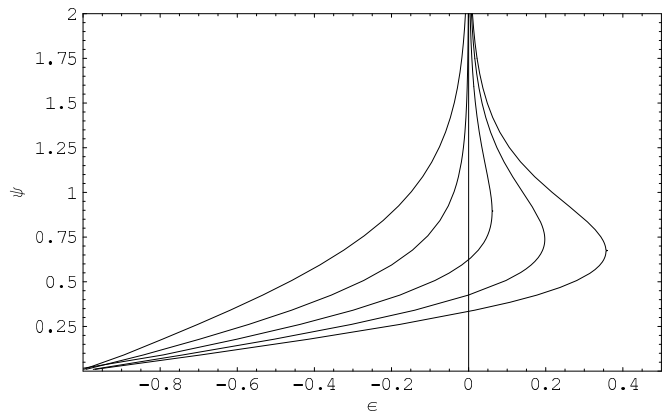


FIG. 21: Relation between  $\psi$  and  $\epsilon$  for  $a = 0.2M$ ,  $\mu_o = 0$ ,  $\eta = \pi/4$ . From left to right, the curves are drawn for  $r_s = 2M, 3M, 4M, 5M, 6M$  respectively. Note that for these values we have  $r_m = 3.16M$ .

sumes a key role in their success. This variable is defined by the relation

$$2K(k)\psi = a\mu_- I_1(\epsilon, \eta) + \text{sign}[\eta]F(\lambda_o, k). \quad (\text{A36})$$

The variable  $\psi$  is directly defined in terms of the radial integral  $I_1$ , thus eliminating the problems of the two branches that this function has when is expressed in terms of  $\epsilon$ . The reason behind the coefficient  $2K(k)$  will be clear later.

In Fig. 21 we plot  $\psi$  vs  $\epsilon$  for a generic choice of the parameters. We note that when  $r_s < r_m$ ,  $\epsilon < 0$  for all values of  $\psi$ , whereas for  $r_s > r_m$   $\epsilon$  reaches the maximum value  $\epsilon_{max}$ , corresponding to  $r_s = r_*$  and then tends to zero for very large values of  $\psi$ . On the other hand,  $\epsilon$  is a single-valued function of  $\psi$ . Therefore, we can replace all occurrences of  $\epsilon$  by  $\epsilon(\psi)$  obtained by solving Eq. (A36) numerically.

Multiplying Eq. (A1) by  $a\mu_-$ , separating the  $\mu_s$  term and applying the Jacobi elliptic function  $\text{sn}$ , we get

$$\mu_s = \text{sign}[\eta]\mu_+ \text{sn}[2K(k)\psi, k], \quad (\text{A37})$$

which represents the lens equation for the polar coordinate  $\mu_s$ .

The Jacobi elliptic function  $\text{sn}(x, k)$  is periodic in  $x$  with period  $4K(k)$ . It tends to the usual trigonometric  $\sin$  when  $k$  is small (which is more or less our case, since  $\mu_+ < \mu_-$ ). So, the right hand side of Eq. (A37) vanishes at  $\psi = m$  with  $m$  integer, is maximum at  $\psi = 2m + 1/2$ , and minimum at  $\psi = 2m + 3/2$ . The interval in which there are  $m$  inversion points in the polar motion is  $m - 1/2 < \psi < m + 1/2$ . As we shall see, the fact that this interval has a trivial form in terms of  $\psi$  for any values of  $m$  is crucial in the search for the critical points of higher order. If we had kept  $\epsilon$ , the definition of the search domain would have been much more problematic. In Ref. [19], the variable  $\psi$  played a similar role, but its definition was restricted to the limit of small black

hole spin. In that case  $\psi$  reduces to the equivalent deflection by a Schwarzschild black hole of the same mass. Eq. (A36) generalizes the former definition and allows a fruitful use of this variable in all the Kerr parameter space.

As regards the azimuthal motion, the extrema of  $\phi$  are  $\phi_i = \phi_s$  and  $\phi_f = \phi_o$ . Recalling that we have set  $\phi_o = 0$ , Eq. (A2) can be written in the form

$$\phi_s = a [I_1(\psi, \eta) - I_2(\psi, \eta)] - J J_2(\mu_s, \psi, \eta). \quad (\text{A38})$$

This is the lens equation for the azimuthal coordinate  $\phi_s$ . Along with (A37), it constitutes the lens mapping for a Kerr black hole in the form of Eqs. (6) and (7).

## 6. Remarks on numerical implementation

Here we give a few technical details regarding the numerical implementation of the algorithm for finding critical curves and caustics.

As input parameters we consider the black hole spin  $a$ , the inclination  $\mu_o$ , the source distance  $r_s$ , the caustic order  $m$  and the value of the variable  $\eta$ . Of course, depending on which kind of plot we want to draw, we may decide to cycle on different variables. For example, by cycling on  $\eta$  keeping all other parameters fixed, we get a cross-section of the caustic surface at fixed source distance. Cycling on  $a$ , while keeping  $\eta$  at some specific value, we may get the position of a cusp (for example) as a function of the black hole spin.

Starting from each set of parameters  $\{a, \mu_o, r_s, m, \eta\}$ , first we calculate  $r_+$  and  $r_-$  by solving Eq.  $\Lambda(r) = 0$

with  $\Lambda(r)$  given by Eq. (A13). Then we find  $r_m$  by Eq. (A14).

For any test value of  $\psi$ , we numerically invert Eq. (A36) to find  $\epsilon$ , keeping track of the branch of  $I_1$  in which we are. If we are in the branch characterized by the presence of the radial inversion point, we also need to calculate  $\delta$  by numerical solution of Eq.  $R = 0$ .

All these equations are solved using the Mathematica FindRoot routine with the secant method. The integrations of  $I_1$  and  $I_2$  are performed using the NIntegrate routine, which works pretty well on the finite domains obtained by changing to the  $z$  integration variable.

At this point, we can evaluate the lens equations (A37) and (A38) to get  $\mu_s$  and  $\phi_s$ , without further effort.

The Jacobian of the lens mapping is obtained by evaluating difference quotients of  $\mu_s$  and  $\phi_s$  with respect to  $\psi$  and  $\eta$ .

Finally, the zero of the Jacobian at fixed  $\eta$  is found by applying the secant method with respect to  $\psi$  in the range  $[m - 1/2, m + 1/2]$ .

Depending on the required precision and the number of points in the cycle, the evaluation of a caustic may take several minutes. We have required a precision of  $10^{-6}$  in  $\psi$  and about 500 points for each caustic, refining the sampling in the neighborhood of the cusps. With this setup, a cross-section at fixed  $r_s$  takes about 5 minutes on a laptop. Numerical noise has been detected on prograde orbits at extremal spin only starting from the fifth order caustic.

- 
- [1] R.P. Kerr, Phys. Rev. Lett. **11**, 237 (1963).
  - [2] S. Chandrasekhar, *Mathematical Theory of Black Holes*, Clarendon Press, Oxford (1983).
  - [3] F. Melia, *The Galactic Supermassive Black Hole*, Princeton U. Press (2007).
  - [4] W. Hasse and V. Perlick, Jour. of Math. Phys. **47**, 042503 (2006).
  - [5] J.P. Luminet, A&A **75**, 228 (1979); S.U. Viergutz, A&A **272**, 355 (1993); R. Takahashi, Astrophys. J. **611**, 996 (2004).
  - [6] K. Beckwith and Ch. Done, MNRAS **352**, 353 (2004); **359**, 1217 (2005).
  - [7] V. Karas, D. Vokrouhlicky, and A.G. Polnarev, MNRAS **259**, 569 (1992).
  - [8] A.E. Broderick and A. Loeb, MNRAS **363**, 353 (2005); **367**, 905 (2006).
  - [9] C.T. Cunningham and J.M. Bardeen, ApJ **183**, 237 (1973).
  - [10] Y. Tanaka, K. Nandra, A.C. Fabian *et al.*, Nat. **375**, 659 (1995).
  - [11] T.P. Krichbaum *et al.*, Proc. 6th European VLBI Network Symposium, Bonn, Germany, astro-ph/0207022.
  - [12] *The Power of Optical/IR Interferometry: Recent Scientific Results and 2nd Generation Instrumentation*, Proceedings of the ESO Workshop held in Garching, Germany, Springer Berlin (2005).
  - [13] H. Falcke, F. Melia, and E. Agol, ApJ **528**, L13 (1999); A. de Vries, Class. Quant. Grav. **17**, 123 (2000); A.E. Broderick and A. Loeb, Journal of Physics, **54**, 448 (2006).
  - [14] P. Schneider, J. Ehlers, E.E. Falco, Gravitational lenses, Springer-Verlag, Berlin (1992).
  - [15] K.P. Rauch and R.D. Blandford, ApJ, **421**, 46 (1994).
  - [16] M. Sereno and F. De Luca, arXiv:0710.5923 (2007).
  - [17] V. Bozza, Phys. Rev. D **66**, 103001 (2002).
  - [18] V. Bozza, F. De Luca, G. Scarpetta, and M.Sereno, Phys. Rev. D **72**, 083003 (2005).
  - [19] V. Bozza, F. De Luca, and G. Scarpetta, Phys. Rev. D **74**, 063001 (2006).
  - [20] V. Bozza and G. Scarpetta, Phys. Rev. D **76**, 083008 (2007).
  - [21] R.H. Boyer and R.W. Lindquist, Jour. of Math. Phys. **8**, 265 (1967).
  - [22] A.F. Zakharov *et al.*, A&A **442**, 795 (2005).
  - [23] M. Sereno and F. De Luca, Phys. Rev. D **74**, 123009 (2006).

- [24] C. Darwin, Proc. of the Royal Soc. of London **249**, 180 (1959).
- [25] D.E. Holz & J.A. Wheeler, ApJ **578**, 330 (2002); E.F. Eiroa & D.F. Torres, Phys. Rev. D **69**, 063004 (2004); V. Bozza & L. Mancini, ApJ **611**, 1045 (2004).
- [26] V. Bozza, Phys. Rev. D **67**, 103006 (2003).
- [27] B. Carter, Phys. Rev. **174**, 1559 (1968).